YITP-16-119

Polyakov loop effects on the phase diagram in strong-coupling lattice QCD

Kohtaroh Miura,[1,2,*] Noboru Kawamoto,[3] Takashi Z. Nakano,[4] and Akira Ohnishi[5]

[1]*Centre de Physique Theorique(CPT), Aix-Marseille University, Campus de Luminy, Case 907, 163 Avenue de Luminy, 13288 Marseille cedex 9, France*
[2]*Kobayashi-Maskawa Institute for the Origin of Particles and the Universe, Nagoya University, Nagoya 464-8602, Japan*
[3]*Department of Physics, Faculty of Science, Hokkaido University, Sapporo 060-0810, Japan*
[4]*KOZO KEIKAKU ENGINEERING Inc., Tokyo 164-0012, Japan*
[5]*Yukawa Institute for Theoretical Physics, Kyoto University, Kyoto 606-8502, Japan*

(Dated: October 31, 2016)

We investigate the Polyakov loop effects on the QCD phase diagram by using the strong-coupling $(1/g^2)$ expansion of the lattice QCD (SC-LQCD) with one species of unrooted staggered quark, including $\mathcal{O}(1/g^4)$ effects. We take account of the effects of Polyakov loop fluctuations in Weiss mean-field approximation (MFA), and compare the results with those in the Haar-measure MFA (no fluctuation from the mean-field). The Polyakov loops strongly suppress the chiral transition temperature in the second-order/crossover region at small chemical potential (μ), while they give a minor modification of the first-order phase boundary at larger μ. The Polyakov loops also account for a drastic increase of the interaction measure near the chiral phase transition. The chiral and Polyakov loop susceptibilities (χ_σ, χ_ℓ) have their peaks close to each other in the second-order/crossover region. In particular in Weiss MFA, there is no indication of the separated deconfinement transition boundary from the chiral phase boundary at any μ. We discuss the interplay between the chiral and deconfinement dynamics via the bare quark mass dependence of susceptibilities $\chi_{\sigma,\ell}$.

PACS numbers: 11.15.Me, 12.38.Gc, 11.10.Wx, 25.75.Nq

I. INTRODUCTION

The phase diagram of Quantum Chromodynamics (QCD) at finite temperature (T) and/or quark chemical potential (μ) [1, 2] provides a deep insight into the Universe. At the few microsecond after the big-bang, a quark-gluon plasma (QGP) is supposed to undergo the QCD phase transition/crossover, which results in confinement of color degrees of freedom and the dynamical mass generation of hadrons. In fact, the first principle calculations based on lattice QCD Monte Carlo simulations (LQCD-MC) indicates the crossover around $T_c = 145 - 195$ (MeV) [3]. In compact star cores, a cold-dense system would appear, where various interesting phases are expected [4–8].

The QCD phase transition can be investigated in the laboratory experiments [9]: Circumstantial experimental evidence at the Relativistic Heavy-Ion Collider (RHIC) in Brookhaven National Laboratory together with theoretical arguments implies that the QGP is created in heavy-ion collisions at $\sqrt{s_{NN}} = 200$ GeV, and recent experiments at the Large Hadron Collider (LHC) in CERN give stronger evidence. Probing the phase diagram at finite μ, in particular the critical point (CP) [10], is a central topic in the on-going and future heavy-ion collision experiments at the Facility for Antiproton and Ion Research (FAIR) at GSI, the Nuclotron-based Ion Collider fAcility (NICA) at JINR, and the beam energy scan program at RHIC [11]. Unfortunately, the first principle studies by LQCD-MC loses the robustness at finite μ due to the notorious sign problem [1, 12–15]. Many interesting subjects, for example, the location of CP, the equation of state (EOS) at high density, are still under debate.

The QCD phase diagram may be characterized by two underlying dynamics, the chiral and deconfinement transitions, which are associated with the spontaneous breaking of the chiral symmetry in the chiral limit and the Z_{N_c} center symmetry of the color SU(N_c) gauge group in the heavy quark mass limit, respectively. The order parameter is the chiral condensate (σ)/Polyakov loop (ℓ) for the chiral/deconfinement transition. Although the Z_{N_c} symmetry is explicitly broken by the quark sector (with a finite or vanishing mass), the Polyakov loops are still important degrees of freedom to be responsible for the thermal excitation of quarks near the chiral phase transition. The interplay between the σ and ℓ is under active scrutiny; the LQCD-MC reports that the chiral and Polyakov loop susceptibilities show their peaks at almost the same temperatures for $\mu = 0$, and the separation of two dynamics is proposed at finite μ in several models [2].

We investigate the QCD phase diagram by using the strong-coupling expansion in the lattice QCD (SC-LQCD), which provides a lattice-based and well-suited framework for the chiral and deconfinement transitions without a serious contamination by the sign problem. The SC-LQCD has been successful since the beginning of the lattice gauge theory [16–19], and revisited after the QGP discovery at RHIC as an instructive guide to the QCD phase diagram [20–33]. It is remarkable that a promising phase diagram structure has been obtained even in the strong-coupling limit ($\beta = 2N_c/g^2 \to \infty$) with mean-field approximation (MFA) [20, 22, 24], and exactly determined based on the Monomer-Dimer-Polymer (MDP) formulation [30] and the Auxiliary Field Monte Carlo simulation [33]. The MFA results are then shown to be capturing the essential feature of the exact phase diagram.

* kohtaroh.miura@cpt.univ-mrs.fr; miura@kmi.nagoya-u.ac.jp

Quark Sec.	w.o. PLoop	w. PLoop, Weiss MFA.	w. PLoop, Haar-Meas. MFA.
LO. **($1/g^0$)**	Damgaard et.al. [42] Fukushima [20] Nishida [22] Kawamoto et.al. [24]	Fukushima [36]	Gocksch et.al. [34] Ilgenfritz et.al. [35] Fukushima [36]
NLO. **($1/g^2$)**	Miura et.al. [25] **Study of PLoop Effects**	μ=0: Nakano et.al. [28] **μ >= 0: Miura et.al. (Present Work)** **Study of PLoop-Fluctuation**	μ=0: Nakano et.al [28] **μ >= 0: Miura et.al. (Present Work)** **Study of NNLO Effects**
NNLO. **($1/g^4$)**	Nakano et.al. [27]	μ=0: Nakano et.al. [28]	μ=0: Nakano et.al. [28] **μ >= 0: Miura et.al. (Present Work)**

FIG. 1: (Color online) The summary of the SC-LQCD studies on the QCD phase diagram for color SU(3) using MFA.

In Fig. 1, we summarize the SC-LQCD studies on the color SU(3) QCD phase diagram using MFA. Based on the success in the strong-coupling limit (top in the second column), we have investigated the phase diagram [25, 27] by taking account of the next-to-leading order (NLO, $\mathcal{O}(1/g^2)$, middle in the second column) and the next-to-next-to-leading order (NNLO,$\mathcal{O}(1/g^4)$, bottom in the second column) of the strong-coupling expansion. The chiral phase transition temperature T_c is strongly suppressed by the NLO effects, and the phase diagram evolves into the empirical shape with increasing lattice coupling $\beta = 2N_c/g^2$, while the NNLO effects give much milder corrections.

In the works mentioned above (listed in the second column of Fig. 1), the main focus was put on the chiral dynamics, rather than the Z_{N_c} deconfinement dynamics, which is another important dynamics described by the Polyakov loops ℓ of the pure-gluonic sector. The SC-LQCD has been well-suited to include both dynamics at the strong-coupling limit [34–36] (top in third and fourth columns in Fig. 1); the strong-coupling limit for the quark sector is combined with the leading-order effect of the Polyakov loops in the pure-gluonic sector and the quark determinant term provides the lattice-based derivation of the σ - ℓ coupling. It is intriguing to include the higher-order of the strong-coupling expansion, which has been carried out in our previous work [28] (middle and bottom lines in third and last columns in Fig. 1); we have shown that the Polyakov loop effects combined with finite lattice couplings β further suppresses the chiral transition temperature T_c, which reproduces the results of LQCD-MC simulations [38–40] at $\mu = 0$ in the certain lattice coupling range $\beta \sim 4$. Thus, the long-standing problem of the SC-LQCD - too large T_c - is greatly relaxed by the Polyakov loops. Moreover, the Polyakov loop sector at the chiral phase transition $\sim \mathcal{O}([1/g^2]^{1/T_c})$ is found to be comparable with the quark sector with NLO $[\mathcal{O}(1/g^2)]$ and NNLO $[\mathcal{O}(1/g^4)]$ at $T_c(\beta \sim 4) \sim 0.5 - 0.6$ (in lattice units); the Polyakov loop effects are necessary to evaluate T_c with respect to the order counting of the strong-coupling expansion.

In our previous paper [28], however, the analysis was limited at vanishing chemical potential $\mu = 0$, while the finite μ region receives a growing interest by the forthcoming experiments focusing the CP and high density phase. The purpose of the present paper is to extend our previous work [28] to the finite μ region, and to investigate the Polyakov loop effects on the whole region of the QCD phase diagram as indicated by red-solid characters in Fig. 1. We adopt two approximation schemes for the Polyakov loops, a simple mean-field treatment (Haar-measure MFA) and an improved treatment with fluctuation effects (Weiss MFA). Through the various comparisons indicated by the arrows in Fig. 1, we elucidate the effect of the Polyakov loop itself, either the effects of the Polyakov loop fluctuations, as well as the higher-order (NNLO) effects of the strong-coupling expansion. In particular, we focus on thermodynamic quantities, which is of great interest in the study of the equation of state for quark matter but has been challenging in SC-LQCD. Moreover, we discuss the interplay between the chiral and deconfinement dynamics at finite μ via the bare quark mass dependence of susceptibilities $\chi_{\sigma,\ell}$.

We employ one species (unrooted) of staggered fermion, which has a $U_\chi(1)$ chiral symmetry in the strong-coupling region and becomes the four flavor QCD with degenerate masses in the continuum limit. We investigate the $U_\chi(1)$ chiral phase transition/crossover at finite T and μ in color SU($N_c = 3$) gauge group in the $3 + 1$ dimension ($d = 3$). Our focus is not necessarily put on quantitative prediction of the realistic phase diagram, but we attempt to clarify which effects make the SC-LQCD phase diagram being closer to realistic one. Such lattice based arguments would be instructive to future LQCD-MC studies on the QCD phase diagram, even though the flavor-chiral structure in the present study is different from the real-life QCD with 2+1 flavors.

This paper is organized as follows: In Sec. II, we explain the effective potential in strong-coupling lattice QCD with Polyakov loop effects. In Sec. III, we investigate the phase diagram and related quantities by using the effective potential. In Sec. IV, we summarize our work and give a future perspective. Appendix A is devoted to the review of the effective potential derivation.

II. STRONG-COUPLING LATTICE QCD WITH POLYAKOV LOOP EFFECTS

We explain the effective potential of the strong-coupling lattice QCD including the Polyakov loop effects. The derivation has been detailed in our previous work [28], and recapitulated in Appendix A in this paper. Here we explain the essential property of the effective potential. We will work on lattice units $a = 1$ in color SU($N_c = 3$) gauge and 3+1 dimension ($d = 3$). The parameters in the effective potential are the lattice coupling $\beta = 2N_c/g^2$, lattice bare quark mass m_0, lattice temperature $T = 1/N_t$ (N_t = temporal lattice extension), and quark chemical potential μ.

The effective potential $\mathcal{F}_{\text{eff}}^{\text{H/W}}$ involves the plaquette-driven Polyakov loop sector $\mathcal{F}_{\text{P}}^{\text{H/W}}$ and the quark sector $\mathcal{F}_{\text{Q}}^{\text{H/W}}$,

$$\begin{aligned}&\mathcal{F}_{\text{eff}}^{\text{H/W}}(\Phi,\ell,\bar{\ell};\beta,m_0,T,\mu)\\&=\mathcal{F}_{\text{P}}^{\text{H/W}}(\ell,\bar{\ell},\beta,T)+\mathcal{F}_{\text{Q}}^{\text{H/W}}(\Phi,\beta,m_0,T,\mu)\\&\quad+\mathcal{O}(1/g^6,1/g^{2(N_t+2)},1/\sqrt{d})\,. \end{aligned} \tag{1}$$

The $\mathcal{F}_{\text{P}}^{\text{H/W}}$ is responsible for the Polyakov loop effects

$$L_p = N_c^{-1}\prod_\tau U_{0,\tau\mathbf{x}}\,,\quad U_0 = \text{temporal link variable}\,, \tag{2}$$

which result from the integral over the spatial link variables for the plaquettes wrapping around the temporal direction. Such Polyakov loops are dubbed “plaquette-driven”, and purely gluonic. The effects of L_p is investigated in two MFA scheme: the Haar measure and Weiss MFA - as indicated by the suffixes “H” and “W”. In the former, the Polyakov loop L_p is simply replaced with its constant mean-field ℓ, while in the latter, the mean-field ℓ is introduced via the extended Hubbard-Stratonovich transformation [25] and the fluctuations from the mean-field is taken account in the integral over the U_0. The Polyakov loop effective potential of Haar measure MFA is well-known since 1980’s [41],

$$\begin{aligned}&\mathcal{F}_{\text{P}}^{\text{H}}(\ell,\bar{\ell},\beta,T)\\&=-2TdN_c^2\left(\frac{1}{g^2N_c}\right)^{1/T}\bar{\ell}\ell-T\log\mathcal{R}_{\text{Haar}}\,,\end{aligned} \tag{3}$$

$$\mathcal{R}_{\text{Haar}}\equiv 1-6\bar{\ell}\ell-3\big(\bar{\ell}\ell\big)^2+4\big(\ell^{N_c}+\bar{\ell}^{N_c}\big)\,, \tag{4}$$

where the Haar measure in the U_0 path integral leads to the Z_3 symmetric term $\mathcal{R}_{\text{Haar}}$. Since the $\mathcal{R}_{\text{Haar}}$ does not couple to the dynamical quarks, the Z_3 symmetry affects the phase diagram separately from the chiral dynamics in Haar measure MFA. In sharp contrast to this, there is no counterpart in Weiss MFA [28],

$$\mathcal{F}_{\text{P}}^{\text{W}}(\ell,\bar{\ell},\beta,T)=2TdN_c^2\left(\frac{1}{g^2N_c}\right)^{1/T}\bar{\ell}\ell\,. \tag{5}$$

The Polyakov loop effects other than the quadratic term (5) are entangled to the dynamical quarks in the quark determinant as explained in the followings. Thus, the Z_3 dynamics is totally spoiled by the dynamical quarks in Weiss MFA.

In both Haar measure and Weiss MFA cases, the order counting of the strong-coupling expansion reads,

$$\mathcal{F}_{\text{P}}^{\text{H/W}}\sim\mathcal{O}((1/g^2)^{N_t=1/T})\,, \tag{6}$$

and thus depends on the lattice temperature $T = 1/N_t$, which is subject to the integer value N_t. However in this paper, we regard T as a continuous valued given number, which naturally follows in the lattice Matsubara formalism [42]. Around the chiral transition/crossover temperature T_c, we will show that the $\mathcal{F}_{\text{P}}^{\text{H/W}}$ becomes comparable to the NLO or NNLO effects: $\mathcal{O}(1/g^{2/T_c})\sim\mathcal{O}(1/g^{2-4})$.

The quark sector $\mathcal{F}_{\text{Q}}^{\text{H/W}}$ in Eq. (1) is derived by integrating out the staggered quarks with link/plaquette variables in each order of the strong-coupling expansion. In this paper, we consider the LO, NLO, and NNLO effects;

$$\mathcal{F}_{\text{Q}}^{\text{H/W}}\ni\mathcal{O}(1/g^0)\,,\mathcal{O}(1/g^2)\,,\mathcal{O}(1/g^4)\,. \tag{7}$$

The integral is evaluated by introducing several auxiliary fields Φ, which includes the chiral condensate σ, the order parameter of the $U_\chi(1)$ chiral symmetry, as well as other fields,

$$\Phi=\left\{\sigma,\psi_\tau,\bar{\psi}_\tau,\psi_s,\bar{\psi}_s,\psi_{\tau s},\bar{\psi}_{\tau s},\psi_{ss},\bar{\psi}_{ss},\psi_{\tau\tau},\bar{\psi}_{\tau\tau}\right\}\,, \tag{8}$$

whose physical meanings are summarized in Tables I and II in the Appendix A. The coefficients of the effective potential terms are solely characterized by (β, N_c, d) and $\mathcal{O}(1/g^{0-4})$ (see Table III). The total quark sector $\mathcal{F}_{\text{Q}}^{\text{H/W}}$ is then divided into the auxiliary field part $\mathcal{F}_{\text{X}}$ and the quark determinant part $\mathcal{F}_{\text{det}}^{\text{H/W}}$. As shown in Eq. (A17) in Appendix A, the $\mathcal{F}_{\text{X}}$ is composed of the quadratic terms of the auxiliary fields Φ.

The quark determinant term $\mathcal{F}_{\text{det}}^{\text{H/W}}$ is responsible for the dynamical quark effects, and includes the quark hoppings with link variables U_0 wrapping around the temporal direction, which give rise to the “quark-driven” Polyakov loops. In Haar measure MFA, the quark determinant part becomes similar to that in the Polyakov-loop-extended Nambu-Jona-Lasinio (PNJL) model [37, 43] [51] and the Polyakov-loop-extended Quark-Meson (PQM) model [44]:

$$\begin{aligned}\mathcal{F}_{\text{det}}^{\text{H}}&=-N_cE_q-N_c\log\sqrt{Z_+Z_-}\\&\quad-T\Big(\log\mathcal{R}_q(E_q-\tilde{\mu},\ell,\bar{\ell})+\log\mathcal{R}_q(E_q+\tilde{\mu},\bar{\ell},\ell)\Big)\,,\end{aligned} \tag{9}$$

$$\mathcal{R}_q(x,y,\bar{y})\equiv 1+N_c(ye^{-x/T}+\bar{y}e^{-2x/T})+e^{-3x/T}\,. \tag{10}$$

See Table IV for the quark excitation energy E_q, the shifted quark chemical potential $\tilde{\mu}$, and the wave function renormalization factor $\sqrt{Z_+Z_-}$. In Weiss MFA, the plaquette-driven and quark-driven Polyakov loops are combined in the quark determinant, and the U_0 path integral accounts for the Polyakov loop fluctuations. Then we obtain the following expression,

$$\mathcal{F}_{\text{det}}^{\text{W}}=-N_c\log\sqrt{Z_+Z_-}-T\log\left[\sum_I\mathcal{Q}^I(\Phi)\mathcal{P}^I(\ell,\bar{\ell})\right]\,, \tag{11}$$

$$\mathcal{P}^I(\ell,\bar{\ell})=\sum_{n=-\infty}^{\infty}\left(\sqrt{\ell/\bar{\ell}}\right)^{-N_cn+N_{\text{B}}^I}\mathcal{P}_n^I\left(\sqrt{\ell\bar{\ell}}\right)\,, \tag{12}$$

where the thermal excitation of a quark and its composite $\mathcal{Q}^I$, the thermal excitation of Polyakov loops $\mathcal{P}_n^I$, and the baryon number index N_{B}^I are summarized in Table V in Appendix A. In the heavy quark limit $m_0 \to \infty$, Eq. (11) recovers the Z_3 symmetry as shown in Appendix A.

The auxiliary fields $\{\Phi, \ell, \bar{\ell}\}$ at equilibrium are determined as a function of (β, m_0, T, μ) via the saddle point search of the effective potential $\mathcal{F}_{\mathrm{eff}}^{\mathrm{H/W}}$. In particular, the important quantities to probe the phase diagram are the chiral condensate $\sigma \in \Phi$, Polyakov loops $(\ell, \bar{\ell})$, and their (dimensionless) susceptibilities (χ_σ, χ_ℓ). In the present mean-field framework, the susceptibilities are evaluated as follows: We consider the curvature matrix C of the effective potential at equilibrium,

$$C_{ij} = \frac{1}{T^4} \frac{\partial^2 \mathcal{F}_{\mathrm{eff}}^{\mathrm{H/W}}}{\partial \phi_i \partial \phi_j}\bigg|_{\mathrm{equilibrium}} , \tag{13}$$

where the field ϕ_i represents the dimensionless auxiliary fields normalized by T and N_c,

$$\phi_i \in \left\{ \frac{\sigma}{T^3 N_c}, \frac{\psi_\tau}{T^3 N_c}, \frac{\bar{\psi}_\tau}{T^3 N_c}, \frac{\psi_s}{T^6 N_c^2}, \frac{\bar{\psi}_s}{T^6 N_c^2}, \frac{\psi_{\tau s}}{T^6 N_c^2}, \frac{\bar{\psi}_{\tau s}}{T^6 N_c^2}, \frac{\psi_{ss}}{T^{12} N_c^4}, \frac{\bar{\psi}_{ss}}{T^6 N_c^2}, \frac{\psi_{\tau\tau}}{T^3 N_c}, \frac{\bar{\psi}_{\tau\tau}}{T^3 N_c}, \ell, \bar{\ell} \right\} . \tag{14}$$

Then the chiral and Polyakov loop susceptibilities are given by

$$\chi_\sigma = (C^{-1})_{ij=\sigma\sigma} , \quad \chi_\ell = (C^{-1})_{ij=\ell\bar{\ell}} . \tag{15}$$

In addition, we investigate thermodynamic quantities, a pressure p, quark number density ρ_q, and interaction measure Δ,

$$p = -\left(\mathcal{F}_{\mathrm{eff}}^{\mathrm{H/W}}(T, \mu) - \mathcal{F}_{\mathrm{eff}}^{\mathrm{H/W}}(0, 0)\right) , \tag{16}$$

$$\rho_q = \frac{\partial p}{\partial \mu} , \tag{17}$$

$$\Delta = \frac{\epsilon - 3p}{T^4} , \tag{18}$$

where $\epsilon = -p + Ts + \mu\rho_q$ represents an internal energy with $s = \partial p / \partial T$ being an entropy.

III. RESULTS

We investigate the QCD phase diagram based on the effective potential explained in the previous section. We show the phase diagram and related quantities obtained in Haar measure MFA at next-to-leading order (NLO) in Subsec. III A, Weiss MFA at NLO in Subsec. III B for the fixed lattice coupling $\beta = 4$ in the chiral limit ($m_0 = 0$). We extend our study to include the finite bare quark mass $m_0 > 0$ in Subsec. III C with a particular focus on the chiral and Polyakov loop susceptibilities. Then, in Subsec. III D, we show the phase diagram evolution for various β. Finally, in Subsec. III E, we study the next-to-next-to-leading order (NNLO) effects in the phase diagram.

A. Haar Measure MFA at NLO

We consider the NLO Haar measure MFA, where the NNLO $\mathcal{O}(1/g^4)$ terms in the coupling coefficients shown in Table III and the Polyakov loop fluctuations are ignored. We concentrate on the chiral limit case $m_0 = 0$. We take the lattice coupling $\beta = 4.0$ as a typical value, for which the chiral transition temperature at vanishing quark chemical potential $T_{c,\mu=0}$ [28] becomes close to the LQCD-MC result [38] (For details on the comparison, see Refs. [28, 31]). The effects ignored or restricted here will be investigated in later subsections. The phase diagram in the Haar measure MFA is partly studied in our previous work [26], and we provide more complete analyses in the followings.

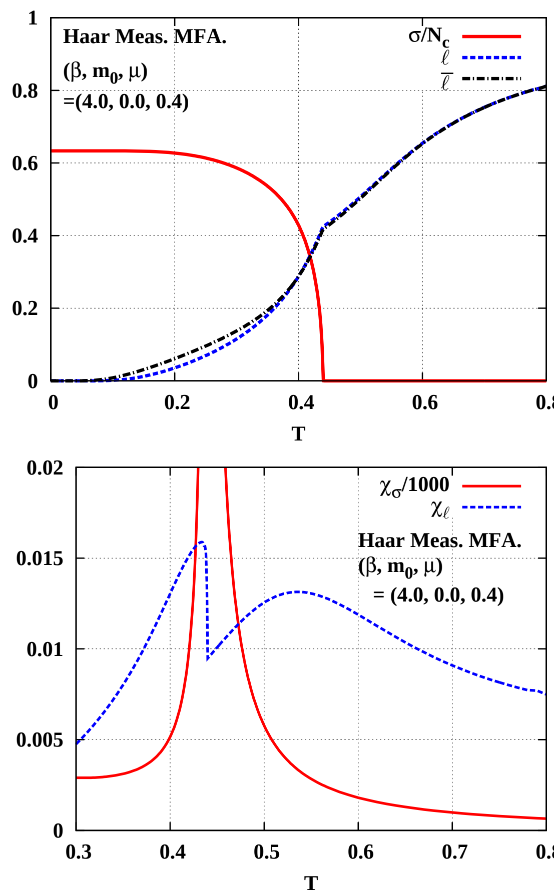

FIG. 2: (Color online) Upper: The chiral condensates σ, Polyakov loops $(\ell, \bar{\ell})$, in NLO Haar Measure MFA as a function of T at $(\beta, m_0, \mu) = (4.0, 0.0, 0.4)$. Lower: The chiral and Polyakov loop susceptibilities (χ_σ and χ_ℓ) in the same condition as the upper panel. For a comparison, the χ_σ is multiplied by 1/1000.

In the upper panel of Fig. 2, we show the chiral condensates (σ/N_c) and Polyakov loops $(\ell, \bar{\ell})$ at finite quark chemical potential $\mu = 0.4$ as a function of temperature T for $(\beta, m_0) = (4.0, 0.0)$. In the low T region, the chiral broken ($\sigma \neq 0$) and confined ($\ell \sim 0$) phase appears. As T increases, we observe the second-order chiral phase transition ($\sigma \to 0$) at $T_c \simeq 0.44$ and the large increase of the Polyakov loops

($\ell \to \mathcal{O}(1)$). These results are similar to the zero chemical potential case shown in the previous study [28].

We find that the Polyakov loop is smaller than the anti-Polyakov loop ($\ell < \bar{\ell}$) in the chiral broken phase. This is understood from a quark screening effect at high density: A finite μ leads to a net quark number density at equilibrium, where putting additional quarks into the system would give a larger energy cost than anti-quarks. Therefore the free energy of the quark gets larger than that of the anti-quark $F_q > F_{\bar{q}}$, which attributes to our observation $\ell < \bar{\ell}$ through the relation $(\ell, \bar{\ell}) \propto (e^{-F_q/T}, e^{-F_{\bar{q}}/T})$.

In the lower panel of Fig. 2, we compare the temperature dependence of the chiral and Polyakov loop susceptibilities (χ_σ, χ_ℓ) which are defined in Eq. (15) in the same condition as the upper panel. The Polyakov loop susceptibility has two peaks with a relatively wide width. We note that the action in the present SC-LQCD (A2) has the $U_\chi(1)$ chiral symmetry, which governs the dynamics of the system. Since the first peak is found in the vicinity of the chiral phase transition, it should be associated with the chiral dynamics. The second peak (or bump) is found in the chiral restored phase $T \simeq 0.53 > T_c$, and interpreted as the remnant of the Z_3 deconfinement dynamics as discussed in the subsection III C.

In the upper panel of Fig. 3, we show the chiral condensates σ/N_c as a function of chemical potential μ for three fixed temperatures $T = 0.15,\ 0.20,\ 0.25$. At $T = 0.25$ (red-solid line), we find the second-order phase transition. At lower $T \sim 0.20$ (blue-dashed line), the chiral symmetry is partially restored with the first-order phase transition as μ increases, and gets completely restored with the second-order phase transition at larger μ. As shown in the previous study [25], the partial chiral restoration (PCR) emerges due to the self-consistent evaluation of the finite β effects for the chemical potential: The *effective* chemical potential appears as an implicit function of σ, $\mu \to \tilde{\mu}(\sigma, \beta) = \mu - \delta\mu(\sigma, \beta)$ (see, Table IV), which allows a stable equilibrium satisfying $\sigma \sim \tilde{\mu}(\sigma)$, leading to the PCR. Our finding in the present study is that the PCR is not spoiled by the Polyakov loop effects, but still exists. As T decreases, the PCR disappears and the first-order chiral transition dominates as indicated by the $T = 0.15$ case (dashed-dotted black line).

In the lower panel of Fig. 3, we pick up the $T = 0.25$ case from the upper panel and show the μ dependence of σ/N_c in a wider range. The Polyakov loops $(\ell, \bar{\ell})$ and the quark number density (ρ_q/N_c defined by Eq. (17)) are also displayed. The Polyakov loops increase in the chiral broken phase $\mu < \mu_c \simeq 0.59$, and the increasing rate stays quite small compared with the finite T transition case. In contrast, the quark number density rapidly increases in the vicinity of the chiral phase transition. After the transition ($\mu \geq \mu_c$), we observe a high density system ($\rho_q \sim N_c$) with a little quark excitation ($\ell \ll 1$). This property as well as the possibility of two sequential transitions associated with the PCR would be reminiscent of the original idea of the quarkyonic phase [5].

In the symmetric phase, the Polyakov loops $(\ell, \bar{\ell})$ start decreasing with the relation $\bar{\ell} < \ell$ as μ increases. This would be a saturation artifact on the lattice: As we explained above, the chiral symmetry restoration leads to a high density system

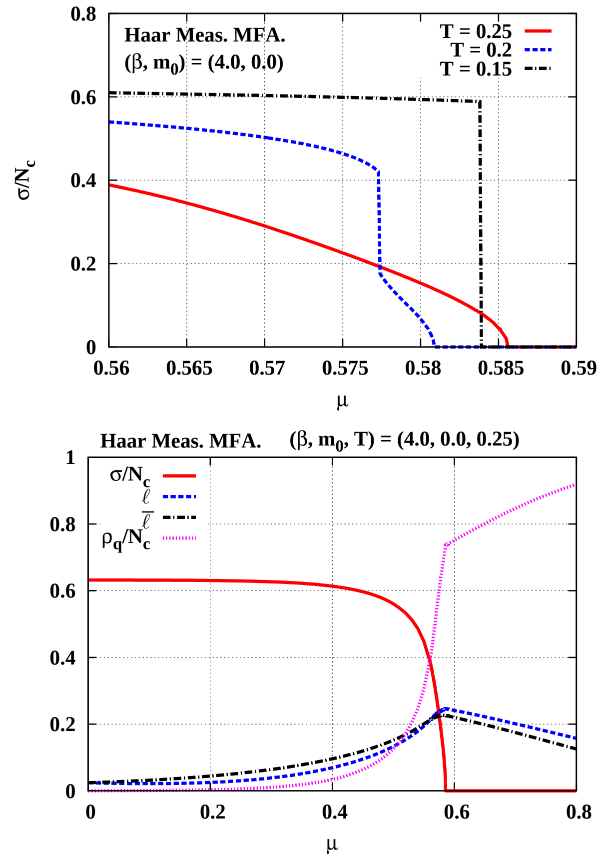

FIG. 3: (Color online) Upper: The chiral condensates σ, Polyakov loops $(\ell, \bar{\ell})$, in NLO Haar Measure MFA as a function of μ at $(\beta, m_0) = (4.0, 0.0)$ for the selected temperatures $T = 0.15,\ 0.2,\ 0.25$. Lower: The σ, $(\ell, \bar{\ell})$, and quark number density ρ_q in NLO Haar Measure MFA as a function of μ at $(\beta, m_0, T) = (4.0, 0.0, 0.25)$.

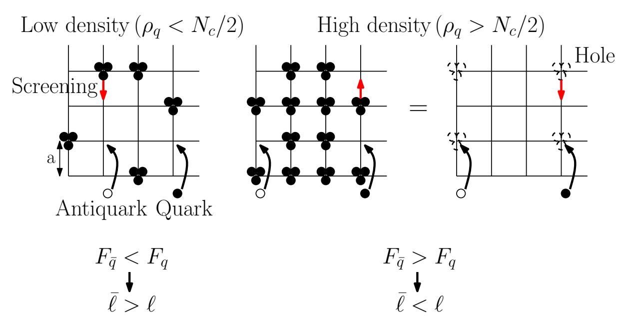

FIG. 4: (Color online) The half-filled and saturation.

$\rho_q > N_c/2$ so that more than half of the lattice sites are filled by quarks. Then the holes - sites without quarks - behave like anti-quarks, and the system with the quark number density $\rho_q > N_c/2$ would be identical to the system with the anti-quark number density $\rho_{\bar{q}} = (N_c - \rho_q) < N_c/2$. Therefore, the excitation property of quarks and anti-quarks becomes opposite ($F_q < F_{\bar{q}}$) as illustrated in Fig 4, and thus $\bar{\ell} < \ell$ holds. As μ becomes larger after the half-filling, the number of holes decreases and the degrees of freedom get frozen. Hence the excitations of both quarks and anti-quarks are suppressed at larger μ, which results in the decreasing trend of $(\ell, \bar{\ell})$ as functions of μ.

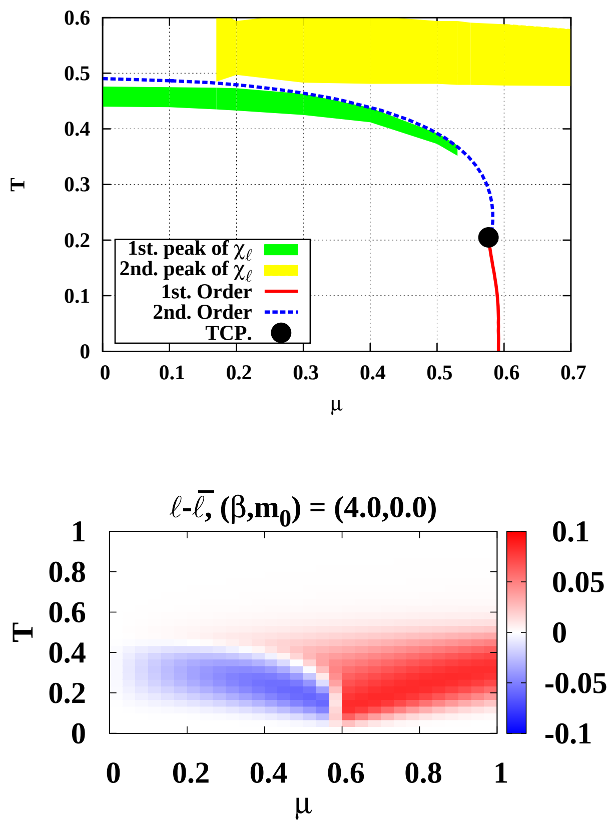

FIG. 5: (Color online) Upper: The phase diagram of NLO Haar Measure MFA at $(\beta, m_0) = (4.0, 0.0)$. See texts for details. Lower: The difference of the Polyakov loop and anti-Polyakov loop in the phase diagram of the NLO Haar measure MFA.

We show the phase diagram of NLO Haar measure MFA in the upper panel of Fig. 5 with $(\beta, m_0) = (4.0, 0.0)$. The first-order chiral phase boundary (red-solid line) emerges in the low T region and ends up with the tri-critical point (TCP, filled black circle) at $(\mu_{\rm TCP}, T_{\rm TCP}) \simeq (0.577, 0.205)$, from which the second-order chiral phase boundary (blue-dashed line) sets in with increasing temperature (The PCR emerges just below the TCP, and invisible in the resolution of Fig. 5. The PCR becomes visible at larger β as seen in Fig. 12). The lower-green (upper-yellow) band corresponds to the width of the Polyakov loop susceptibility χ_ℓ at 90% of its first (second) peak height. The first peak band depends on μ similarly to the chiral phase boundary: As mentioned above, the peak seems to be associated with the chiral phase transition. The peak strength becomes weaker with increasing μ, and disappears at $\mu \simeq 0.53$ before reaching TCP. The second peak is almost independent of μ, and starts appearing in $\mu \gtrsim 0.17$ separately from the first peak.

The phase diagram in the Haar measure MFA is similar to that in PQM [44]: When the μ dependence is absent in the Polyakov loop potential in PQM, the derivative of the Polyakov mean-field in terms of T at finite μ has double peaks, which is analogous to our result shown in the lower panel of Fig. 2 as well as in our previous study [26]. We will revisit this subject in Weiss MFA case in the next subsection.

The lower panel of Fig. 5 shows the difference of the Polyakov loop and anti-Polyakov loop $(\ell - \bar{\ell})$ in the $T - \mu$ plane. The relation $\ell < \bar{\ell}$ holds in the whole $T, \mu > 0$ region in the chiral broken phase as shown by the blue color. The saturation effect $\ell > \bar{\ell}$ is observed as a general tendency at large μ region in the chiral restored phase as indicated by the red color.

As shown in Eq. (6), the plaquette-driven Polyakov loop action includes the $\mathcal{O}(1/g^{2/T})$ correction. At the chiral phase boundary, this effect gives $\mathcal{O}(1/g^{2/T_c}) \lesssim \mathcal{O}(1/g^4)$. For the consistency of the strong coupling expansion, we have to take account of the NNLO $1/g^4$ effects for the quark sector, which will be discussed in the later subsection.

B. Weiss MFA at NLO

We investigate the phase diagram of NLO Weiss MFA, where the Polyakov loop fluctuations from the mean fields $(\ell, \bar{\ell})$ are considered, while the NNLO effects $\mathcal{O}(1/g^4)$ in the coupling coefficients shown in Table III are ignored. We compare the Weiss MFA results with the Haar measure MFA to clarify the effects of the Polyakov loop fluctuations to the phase diagram. We choose the same parameter set as the Haar measure MFA case, $(\beta, m_0) = (4.0, 0.0)$.

As shown in Fig. 6, T or μ dependence of $(\sigma, \ell, \bar{\ell}, \rho_q)$ is qualitatively the same as the Haar measure MFA results. In the following, we concentrate on the results which are characteristic of the Weiss MFA.

In Fig. 7, we show the chiral and Polyakov loop susceptibilities (χ_σ, χ_ℓ) at finite chemical potential $\mu = 0.4$ as a function of temperature T. Two peaks are almost degenerated, and the width of χ_ℓ is sharper than the Haar measure MFA case. We do not see the second (Z_3 associated) peak in the chiral symmetric phase in sharp contrast to the Haar measure MFA case.

In Fig. 8, we show the phase diagram of NLO Weiss MFA with $(\beta, m_0) = (4.0, 0.0)$. We find two qualitative differences between the NLO Weiss MFA and NLO Haar measure MFA results: First, the peak of χ_ℓ (green-band showing the width of χ_ℓ at 90% of the peak height) is more strongly locked to the chiral phase boundary in Weiss MFA than the Haar measure MFA case. Second, the remnant of the Z_3 dynamics such as the yellow band in Fig. 5 does not appear at any μ in the Weiss MFA case. As explained after Eq. (5) in the previous section, the plaquette-driven Polyakov loops are combined into the quark determinant and coupled to the dynamical quark effects via the U_0 path integral. Then, the Weiss MFA does not admit the remnant of the Z_3 symmetry in sharp contrast to the Haar measure MFA and many other chiral effective models [37, 43, 44]. It is sometimes argued that the chiral and deconfinement dynamics might be separated at finite μ [2], but the Weiss MFA does not support the isolated deconfinement

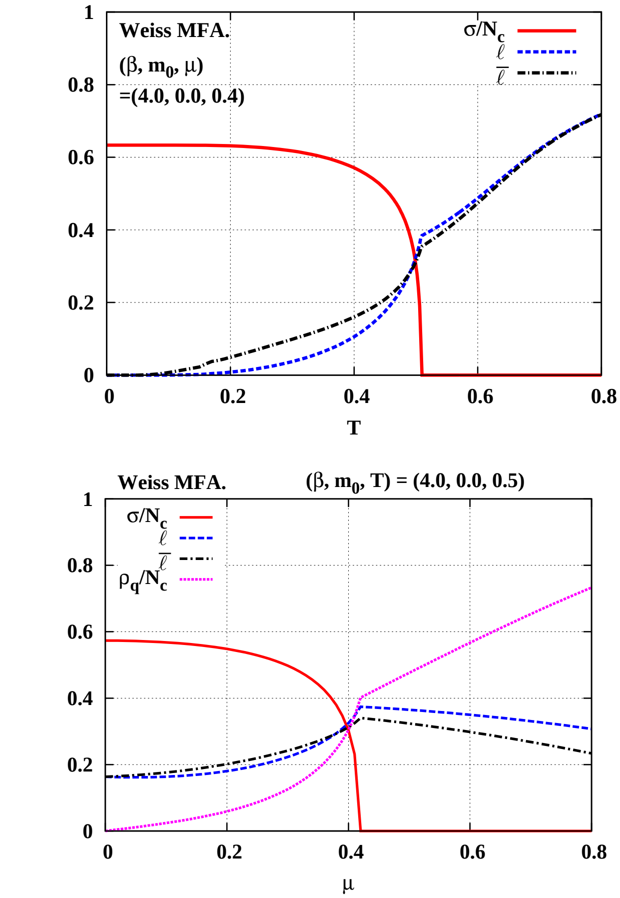

FIG. 6: (Color online) Upper: The chiral condensates σ, Polyakov loops $(\ell, \bar{\ell})$, in NLO Weiss MFA as a function of T at $(\beta, m_0, \mu) = (4.0, 0.0, 0.4)$. Lower: The chiral condensates σ, Polyakov loops $(\ell, \bar{\ell})$, and quark number density ρ_q/N_c in NLO Weiss MFA as a function of μ at $(\beta, m_0, T) = (4.0, 0.0, 0.5)$.

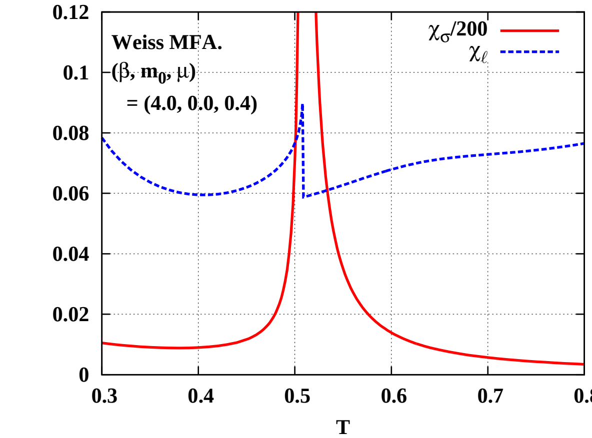

FIG. 7: (Color online) The chiral and Polyakov loop susceptibilities (χ_σ, χ_ℓ) in NLO Weiss MFA as a function of T at $(\beta, m_0, \mu) = (4.0, 0.0, 0.4)$. For a comparison, the chiral susceptibility χ_σ has been multiplied by 1/200.

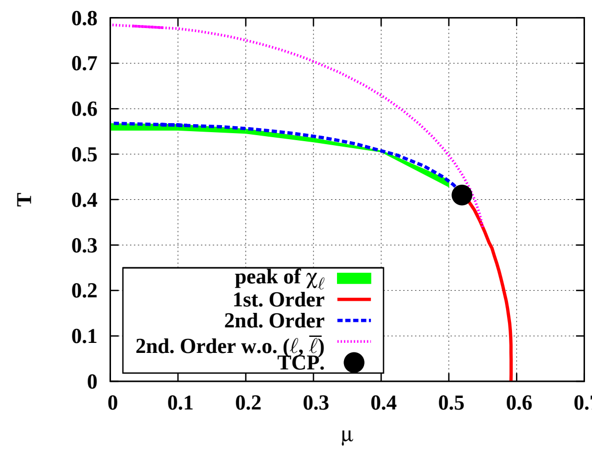

FIG. 8: (Color online) The phase diagram at $(\beta, m_0) = (4.0, 0.0)$ in NLO with Weiss MFA. See texts for details.

dynamics from the chiral phase boundary.

Here, we comment on the recent phase diagram study by the PQM model [44]. In this model, a μ dependence was assumed in the Polyakov loop effective potential based on the phenomenological insights to describe the back reaction of the quark-matter to the Polyakov loops at finite density. This prescription led to a stronger locking between the peak of $d\ell/dT$ and the chiral crossover line, and the double peak structure of $d\ell/dT$ disappeared. These phenomena would be analogous to our findings in the Weiss MFA. We stress that the Weiss MFA effective potential directly results from the path integral in the lattice QCD without additional assumptions. This would be the advantage of the SC-LQCD based effective potential.

We shall consider the formal limit $(\ell, \bar{\ell}) \to 0$ in the effective potential of Weiss MFA $\mathcal{F}_{\rm eff}^{\rm W}$: In the second line of Eq. (11), the thermal excitations (see Table V) carrying a baryon number 0 ($I = \mathrm{MMM}, \mathrm{MQ\bar{Q}}$) and ± 3 ($I = \mathrm{B}, \bar{\mathrm{B}}$) remains and the $\mathcal{F}_{\rm eff}^{\rm W}$ reduces into the effective potential which has been derived in our previous study [25]. We express the reduced effective potential as $\mathcal{F}_{\rm eff}^{\rm NLO}$, and the results obtained by using $\mathcal{F}_{\rm eff}^{\rm NLO}$ will be referred to as *NLO without Polyakov loops* in the later discussions. See Eq. (A24) for the expression of $\mathcal{F}_{\rm eff}^{\rm NLO}$. Needless to say, the $\mathcal{F}_{\rm eff}^{\rm NLO}$ does not implement the Polyakov loop dynamics. By comparing the Weiss NLO MFA and the NLO without Polyakov loops, the Polyakov loop effects become more transparent.

In Fig. 8, we compare the chiral phase boundary of the NLO Weiss MFA and the NLO without Polyakov loops. The second-order phase boundary of the NLO Weiss MFA (blue-dashed line) is found in lower T region than that of NLO without Polyakov loop (magenta-dotted line). As μ becomes larger, two phase boundaries get closer to each other and degenerate in the vicinity of the TCP. The first-order phase boundary is almost independent of the Polyakov loop effects. This is understood as follows. As explained in the previous section, the plaquette-driven Polyakov loops gives the contribution of $\mathcal{O}([1/g^2]^{1/T_c(\mu)})$. At larger μ, this factor decreases because the $T_c(\mu)$ does, and thus the Polyakov loop effects becomes higher order effects of the strong-coupling expansion, and thereby suppressed.

Compared with the Haar measure MFA, the transition temperature $T_c(\mu)$ in the Weiss MFA becomes somewhat larger. Then, the effect of the the plaquette-driven Polyakov loops for $\beta = 4.0$ is maximally $\mathcal{O}([1/g^2]^{1/T_c(\mu=0)}) = \mathcal{O}(1/g^{3.3})$, which is larger than the NNLO effects $1/g^4$. Thus, the present NLO approximation for the quark sector is consistent with respect to the order counting of the strong coupling expansion, at least for $\beta \lesssim 4.0$.

Next, we investigate the thermodynamic quantities in the Weiss MFA. In the upper panel of Fig. 9, we show the normalized pressure p/T^4 as a function of T at chemical potential $\mu = 0.4$, the same condition as Fig. 7. In NLO Weiss MFA, the p/T^4 (red-solid line) becomes significantly larger at $T \gtrsim T_c \simeq 0.507$ and closer to the Stefan-Boltzmann result

$$\frac{p_{\rm sb}}{T^4} = \frac{N_f N_c}{6}\left[\frac{7\pi^2}{30} + \frac{\mu^2}{T^2} + \frac{1}{2\pi^2}\frac{\mu^4}{T^4}\right] + \frac{(N_c^2-1)\pi^2}{45} \,. \tag{19}$$

We do not see such a large enhance of p/T^4 in the case of NLO without Polyakov loops (blue-dashed line). Thus, the Polyakov loop plays an essential role to realize the pressure enhancement which is expected in the QGP phase at high T. More specifically, the pressure enhancement is attributed to the increase of Polyakov loop thermal excitations $\mathcal{P}_n^I(\sqrt{\ell\bar{\ell}})$ (see Table V) included in the Weiss MFA effective potential (11)-(12). This result should be compared with that in the PQM model, where the pressure is rather suppressed by Polyakov loops [44]. The different role of Polyakov loops is understood as follows. Considering the Polyakov loop effects in SC-LQCD meands introducing deconfinement (quark thermal excitation) degrees of freedom as explained above. In contrast, the Polyakov loops act as confinement degrees of freedom in PQM and PNJL models.

In the middle panel of Fig. 9, we show the interaction measure Δ as a function of T at chemical potential $\mu = 0.4$. In NLO Weiss MFA, the Δ has a large peak in the vicinity of the chiral phase transition $T \sim T_c$ as expected with regards to the increasing scale asymmetry in the strongly interacting quark-gluon plasma (sQGP). This should be compared with the result obtained in NLO without Polyakov loops (dashed-blue line) staying small and showing just a tiny bump structure at $T \sim T_c$. In the lower panel of Fig. 9, we compare our results on the interaction measure at vanishing of chemical potential with those obtained in the Monte Carlo simulations (four flavor, the chiral limit is taken) [40]. The Monte Carlo results (green boxes) show the drastic increase in the vicinity of the chiral phase transition. This feature is qualitatively reproduced by the NLO Weiss result (red-solid line), but not in the NLO without Polyakov loops (blue-dashed line). Our results indicate that the Polyakov loops have a large contribution to the scale asymmetry expected in the sQGP.

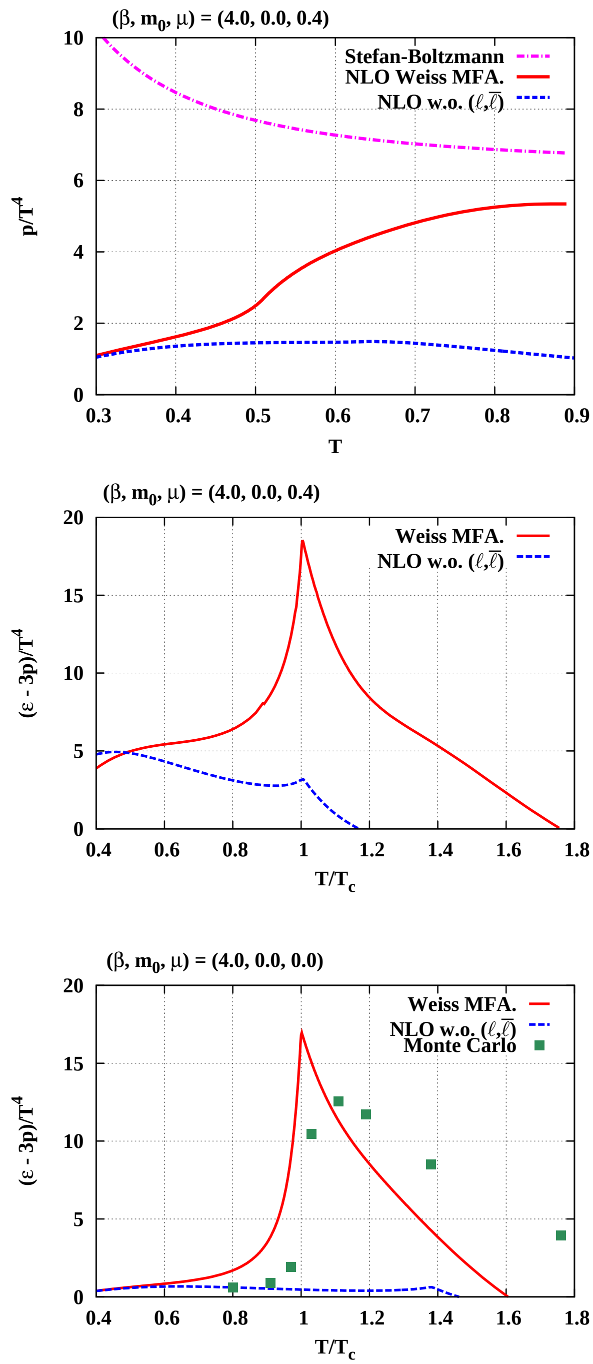

FIG. 9: (Color online) The pressure (upper) and interaction measure (middle and lower) normalized by T^4 in "NLO Weiss MFA" and "NLO without Polyakov loops" as a function of T at $(\beta, m_0, \mu) = (4.0, 0.0, 0.4)$ (upper and middle), and $(\beta, m_0, \mu) = (4.0, 0.0, 0.0)$ (lower). In the lower panel, we have quoted the Monte Carlo results [40].

C. Quark mass dependence

In the previous subsections, we have studied the phase diagram in the chiral limit $m_0 = 0$. In this subsection, we investigate the m_0 dependence of the chiral and Polyakov loop susceptibilities. We choose the same parameter set of $\beta = 4.0$ and $\mu = 0.4$ as previous subsections.

In the upper panel of Fig. 10, we show the chiral suscepti-

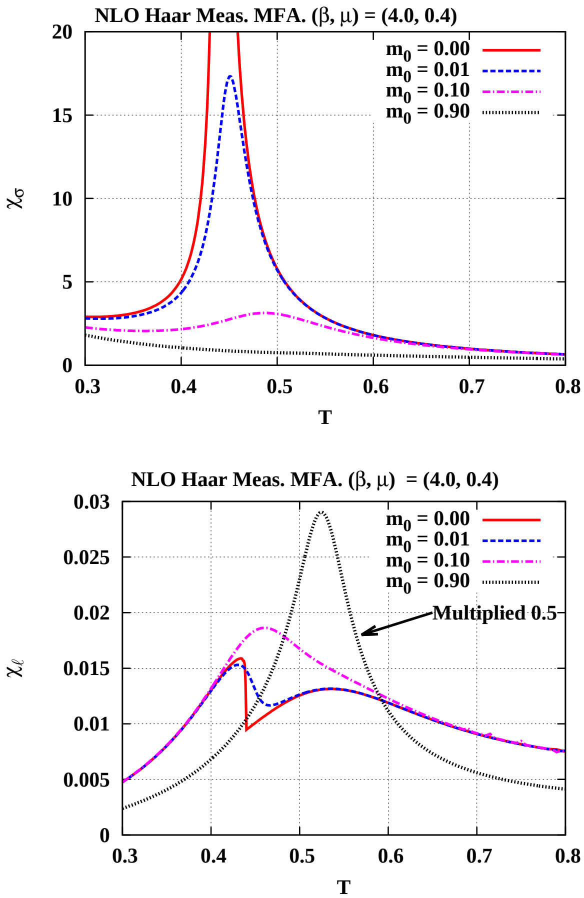

FIG. 10: (Color online) The chiral (upper) and Polyakov loop (lower) susceptibilities as a function of T for various bare quark mass m_0 at $(\beta, \mu) = (4.0, 0.4)$ in NLO Haar measure MFA.

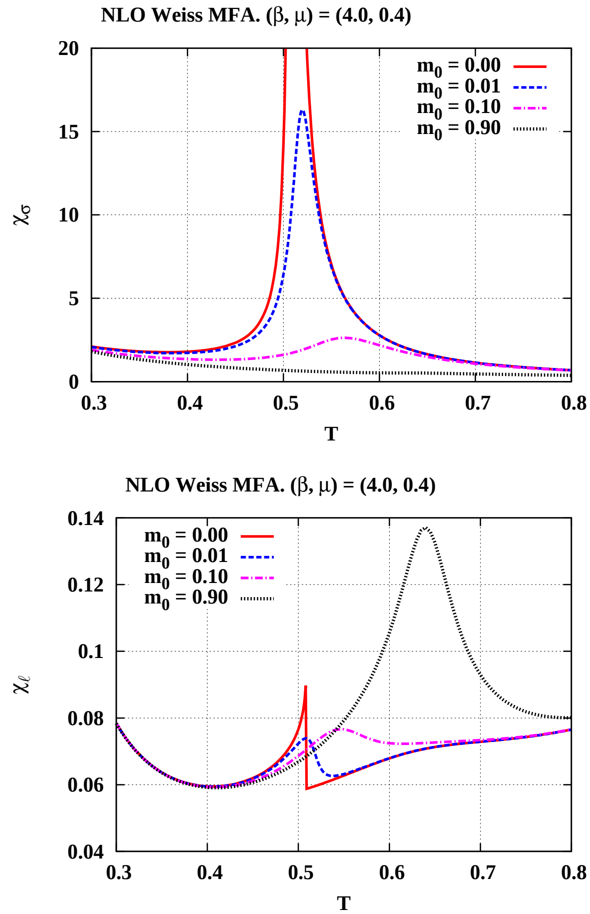

FIG. 11: (Color online) The chiral (upper) and Polyakov loop (lower) susceptibilities as a function of T for various bare quark mass m_0 at $(\beta, \mu) = (4.0, 0.4)$ in NLO Weiss MFA.

bility χ_σ of the NLO Haar measure MFA as a function of T for various bare quark mass m_0 at $(\beta, \mu) = (4.0, 0.4)$. The peak position defines the chiral crossover temperature at finite m_0. The chiral dynamics becomes weaker as indicated by the attenuating peak with increasing m_0. In the lower panel of Fig. 10, we show the Polyakov loop susceptibility χ_ℓ in the same condition as the upper panel. The double peak structure which we have shown in the chiral limit in Subsec III A evolves into a single peak with increasing m_0. The single peak grows up in the heavy mass region $m_0 = 0.9$, and comes to be responsible for the Z_3 crossover. Consistently, the chiral susceptibility does not show any signal there as shown in the upper panel.

We notice that the Z_3 peak of χ_ℓ at $m_0 = 0.9$ locates at the almost same temperature as the second peak appearing in the small mass region $m_0 \lesssim 0.01$. This implies that the second peak originates from the remnant of the Z_3 dynamics. In fact, the approximate Z_3 symmetry remains even in the chiral limit in the effective potential of the Haar measure MFA: The Z_3 symmetric (Haar measure) term $\mathcal{R}_{\rm Haar}$ in Eq. (4) has a large contribution and does not couple to the dynamical fermion effects $\mathcal{R}_q$ in Eq. (A18), so that the former effect is not horribly spoiled by the latter. The result is consistent with our previous work [26].

This should be compared with NLO Weiss MFA results, Fig. 11. The chiral susceptibility χ_σ (upper panel) is qualitatively the same as the Haar measure result, while the Polyakov loop susceptibility χ_ℓ (lower panel) differs: The Weiss MFA does not lead to the double-peak structure in χ_ℓ for any m_0. Thus, the scenario with the double-peak, or equivalently, the deconfinement seperated from the chiral phase boundary at high density would be less supported within the present approximation. To extract a definite conclusion on the relation between two susceptibilities $\chi_{\sigma,\ell}$, we need to investigate the higher-order effects on the Polyakov loops.

It is worth mentioning that the Polyakov loop effective potential in the Haar measure MFA, Eq. (3) is similar to one of the popular choices of the potential in the PNJL model [37, 43] or PQM models. They could in principle contain the remnant of Z_3 dynamics as the Haar measure MFA does. As explained in the previous subsection, the recent work based on PQM assumed a certain μ dependence to the coefficients in the Polyakov loop effective potential [44]. This gives a phenomenological implementation of a back reaction from dynamical quark effects. The Weiss MFA effective potential (especially Eq. (11)) proposes the lattice QCD based solution for the quark back reaction to the Polyakov loops, and opens a possibility to upgrade the PNJL and PQM models so that they account for the Polyakov loop and quark degrees of freedom more systematically. To invent such a model based on the Weiss MFA should be one of the future works.

D. Phase diagram evolution with increasing β

So far, we have studied the phase diagram at a fixed coupling, $\beta = 4.0$. In this subsection, we investigate the phase diagram for various lattice coupling ranging $0.0 \leq \beta \leq 6.0$, while we keep the vanishing bare quark mass $m_0 = 0$. For the chiral phase transition temperature at vanishing chemical potential $T_{c,\mu=0}$, the lattice MC data with one species of staggered fermion are available [30, 38–40] and are compared with $T_{c,\mu=0}$ evaluated in the strong-coupling expansion [25, 27, 28]. We extend our analyses up to $\beta = 6.0$, for which the physical scale of (T_c, μ_c) can be extracted by utilizing the lattice spacing result in Ref. [45].

In the upper panel of Fig. 12, we show the phase diagram evolution with increasing β in the case of NLO Haar measure MFA. In the whole range of $0.0 \leq \beta \leq 6.0$, the chiral phase transition is a first-order in the low temperature region, and it evolves into the second-order at higher T via TCP. The transition temperature at $\mu = 0$ ($T_{c,\mu=0}$) acquires much larger modification with increasing β than the transition chemical potential at $T = 0$ ($\mu_{c,T=0}$). Resultantly, the ratio $R = \mu_{c,\mathrm{T}=0}/T_{c,\mu=0}$ which characterize the shape of the chiral phase boundary is greatly enhanced. For $\beta \geq 4$, the first-order transition line goes inside of the second-order transition line near the TCP, and the PCR explained in the previous subsection emerges between two lines.

In the lower panel of Fig. 12, we show the phase diagram evolution of the NLO Weiss MFA in the chiral limit $m_0 = 0.0$. The results are qualitatively same as the Haar Measure MFA case.

We compare the ratio $R = \mu_{c,\mathrm{T}=0}/T_{c,\mu=0}$ of NLO Weiss MFA to that obtained in the "NLO without Polyakov loops". At $\beta = 4.0$ (6.0), the former (red-solid line) in Fig. 13 becomes 1.38 (1.46) times larger than the latter (blue-dashed line). Thus the ratio R becomes larger by the Polyakov loop effects. Next, we compare our R with those obtained by the Monomer-Dimer-Polymer (MDP) simulation [31]. The MDP (green triangles in Fig. 13) gives a somewhat larger R than our MFA result in the strong-coupling limit, and becomes closer to the NLO Weiss MFA at finite β. The increasing R at larger β is a common trend in both MFA and MDP, and preferable to be consistent with a realistic QCD phase diagram.

In both Haar measure MFA and Weiss MFAs, the TCP tends to go into low T region with increasing β, and the second-order chiral phase boundary becomes dominant. This trend is also reported in the MDP simulations [31, 32] and supports the recent LQCD-MC results based on the critical surface analysis [46]. However, the trend is opposite to the anomaly based expectation for $N_f = 4 > 2$ [47]. This subject should be further discussed with a special care for the anomaly in the staggered fermion formalism.

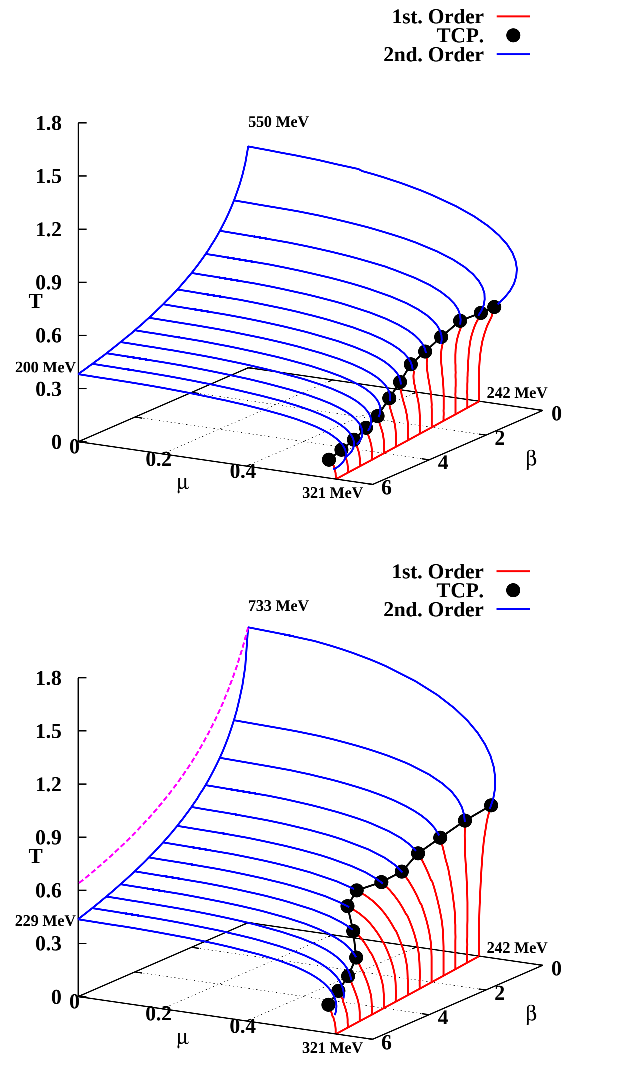

FIG. 12: (Color online) The phase diagram evolution with the increasing lattice coupling β at NLO Haar measure (upper) and Weiss (lower) MFA in the chiral limit. We have quoted $a^{-1}(\beta = 0) = 440$ (MeV) and $a^{-1}(\beta = 6) = 524$ (MeV) from Ref. [45]. In Weiss MFA (lower), we have also shown our previous result on the transition temperature at $\mu = 0$ without effects of plaquette-driven Polyakov loops [25] by the magenta-dashed line.

Finally, we estimate the (T_c, μ_c) in physical units by quoting the lattice spacing scale $a^{-1}(\beta = 0) = 440$ (MeV) and $a^{-1}(\beta = 6) = 524$ (MeV) from the zero temperature strong-coupling expansion [45]. In Haar measure MFA, we find $(T_{c,\mu=0}, \mu_{c,T=0}) \simeq (550, 242)$ (MeV) in the strong-coupling limit, and $(T_{c,\mu=0}, \mu_{c,T=0}) \simeq (200, 321)$ (MeV) at $\beta = 6$. In Weiss MFA, we find $(T_{c,\mu=0}, \mu_{c,T=0}) \simeq (733, 242)$ (MeV) in the strong-coupling limit, and $(T_{c,\mu=0}, \mu_{c,T=0}) \simeq (229, 321)$ (MeV) at $\beta = 6.0$. Although the flavor-chiral structure of the present system differs from the real-life QCD, it is still interesting that the transition temperature of SC-LQCD gets closer

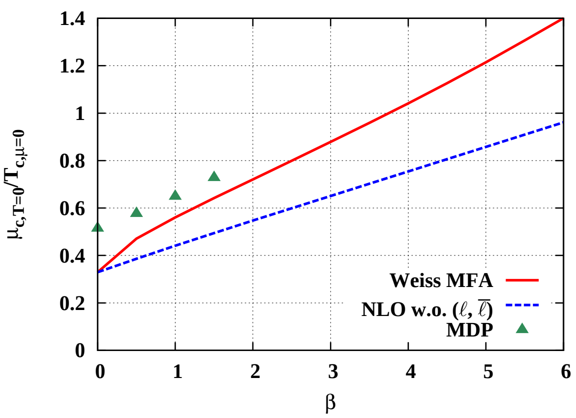

FIG. 13: (Color online) The ratio $R = \mu_{c,T=0}/T_{c,\mu=0}$ as a function of the lattice bare coupling $\beta = 2N_c/g^2$. For a comparison, we show the MDP results for R in Ref. [31]: We read off the $\mu_{c,T=0} \simeq 0.72$ from Fig. 6 in Ref. [31], and quoted the $T_c(\beta)$ evaluated by using the "exponential extrapolation" to calculated the R.

to the realistic one $T_c^{\rm MC} = 145 - 195$ MeV [3].

E. Haar Measure MFA at NNLO

We investigate the phase diagram in the NNLO Haar measure MFA, where the $\mathcal{O}(1/g^4)$ terms in the coupling coefficients (Table III) are considered. We adopt the same parameter set $(\beta, m_0) = (4.0, 0.05)$ as that adopted in the previous work [28]. We investigate the property of the chiral condensates and the Polyakov loops at intermediate and high density region: $\mu = 0.4$ and 0.7. We compare the NNLO phase diagram with the NLO one, and studies the impact of the NNLO corrections.

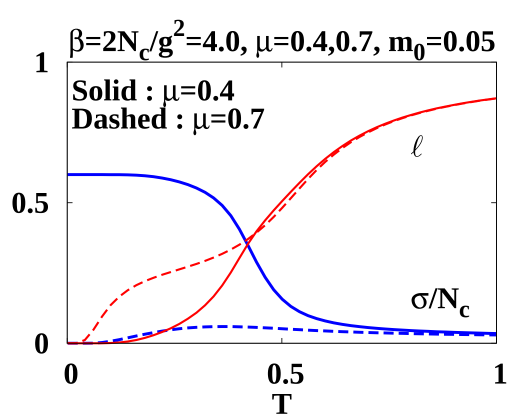

FIG. 14: (Color online) Chiral condensates and Polyakov loops in the NNLO Haar measure MFA. with $m_0 = 0.05$ as a function of temperature at the two chemical potentials $\mu = 0.4$ and 0.7.

In Fig. 14, we show the chiral condensate and Polyakov loop as a function of T. First, we consider the $\mu = 0.4$ cases. At low T, the chiral symmetry is spontaneously broken ($\sigma/N_c \gg m_0 = 0.05$, blue-solid line), and the quarks are confined ($\ell \ll \mathcal{O}(1)$, red-solid line). At high T, the chiral symmetry gets restored up to the finite bare mass effect ($\sigma/N_c \to \mathcal{O}(m_0) \sim 0.05$), and the quarks becomes deconfined ($\ell \sim \mathcal{O}(1)$). The chiral condensate rapidly but smoothly decreases with increasing T, which indicates the chiral crossover rather than the phase transition. At larger chemical potential $\mu = 0.7$, the chiral condensate (blue-dashed line) is small and comparable to the bare quark mass $m_0 = 0.05$ in all T region, and thus the chiral crossover is absent. The chiral susceptibility χ_σ provides the better probe of the chiral dynamics in the crossover region. Figure 15 shows the χ_σ as a function of temperature at $\mu = 0.4$ and 0.7. At $\mu = 0.4$, we find the peak which defines the chiral crossover temperature, while at $\mu = 0.7$, the crossover/peak disappears.

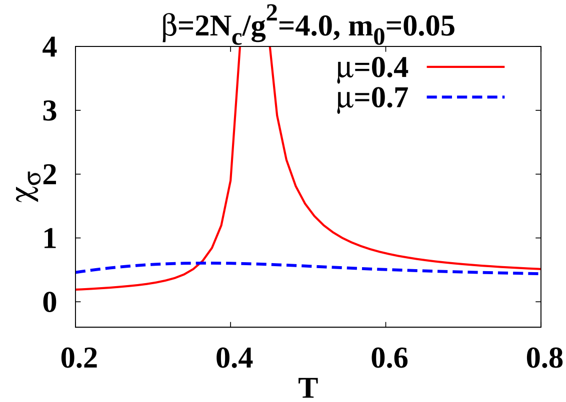

FIG. 15: (Color online) The chiral susceptibility in NNLO Haar measure MFA with $m_0 = 0.05$ as a function of temperature at $\mu = 0.4$ and 0.7.

In Fig. 14, we find the clear difference in the Polyakov loop ℓ at $\mu = 0.7$ and 0.4; the former (red-dashed line) starts increasing even at a tiny (non-zero) temperature where the latter (red-solid line) still remains small. This can be understood in terms of the presence/absence of the spontaneous breaking of the chiral symmetry; at $\mu = 0.4$, the broken chiral symmetry leads to the dynamical quark mass and suppresses the thermal excitation of the quarks, while at 0.7, there is no suppression due to the symmetry restoration. Thus, the relatively large ℓ at low temperature can be a characteristic feature at high density phase. At higher T, ℓ at $\mu = 0.7$ becomes comparable with that at $\mu = 0.4$.

In Fig. 16, we show the temperature derivative of the chiral condensate and Polyakov loop as a function of temperature at $\mu = 0.4$ and 0.7. At $\mu = 0.4$ (solid lines), the chiral and deconfinement crossovers almost simultaneously take place as indicated by their peak positions. This property has been observed at $\mu = 0$ [28]. Our finding here is that the locking of the chiral and deconfinement crossovers remains intact at finite μ as long as the spontaneous symmetry breaking exists. At $\mu = 0.7$, $d(\sigma/N_c)/dT$ (blue-dashed line) shows no signal at any T due to the absence of the chiral crossover, and the

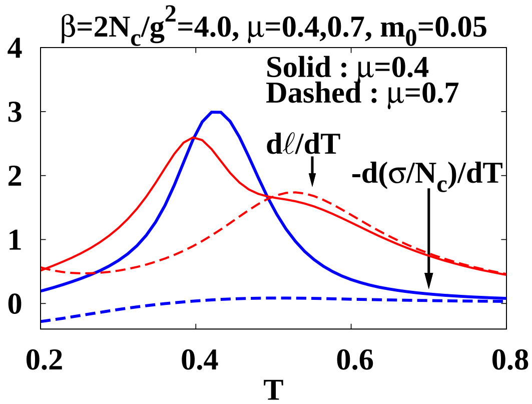

FIG. 16: (Color online) The temperature derivative of the chiral condensates and Polyakov loops in the NNLO Haar measure MFA with $m_0 = 0.05$ as a function of temperature at $\mu = 0.4$ and 0.7.

$d\ell/dT$ (red-dashed line) tends to lose peak-like structure.

In our previous studies [28], we have shown that the NNLO effects to the chiral phase transition/crossover at $\mu = 0$ are very small. We shall now investigate the impact of the NNLO effects to the phase diagram including finite μ. In the left panel of Fig. 17, we show the phase diagram evolution as a function of β in NNLO Haar measure MFA. The red-line represents the critical point evolution and separates the chiral crossover region (higher T) and the first-order transition region (lower T). Due to the finite coupling effects, the crossover line and the critical point move in the lower T direction. For comparison, we show the counterpart at NLO with $m_0 = 0.05$ in the right panel. It is seen that the NNLO phase diagram (left) is very close to the NLO one (right).

In the end of the subsection III A, we have mentioned that the NNLO effects for the quark sector should be included, particularly in the Haar measure MFA, to be consistent with the plaquette-driven Polyakov loop sector with respect to the order counting of the strong-coupling expansion. However, the results in this subsection indicate that the NNLO corrections are tiny in whole region of the phase diagram. Thus, the NLO results shown in the previous subsections would be reliable.

IV. SUMMARY

We have investigated the QCD phase diagram in color SU($N_c = 3$) gauge group at finite temperature T and quark chemical potential μ by using the strong-coupling expansion of the lattice QCD (SC-LQCD) with one species of staggered fermion. Our effective potential [28] includes the LO [$\mathcal{O}(1/g^0)$], NLO [$\mathcal{O}(1/g^2)$], and NNLO [$\mathcal{O}(1/g^4)$] effects of the strong-coupling expansion in the quark sector, and the LO effects of Polyakov loop $\mathcal{O}([1/g^2]^{1/T})$ in the pure gluonic sector. The Polyakov loops are evaluated in two approximation schemes; a simple mean-field treatment (Haar measure mean-field approximation (MFA)) and an improved treatment with fluctuation effects (Weiss MFA). In this setup, we have investigated the whole structure of the SC-LQCD phase diagram with a special emphasis on the Polyakov loops effects.

In both Haar measure and Weiss MFA schemes, the first-order chiral phase boundary emerges in the low T region and ends up with the tri-critical point (TCP), from which the second-order chiral phase boundary evolves to the smaller μ direction with increasing T in the chiral limit ($m_0 = 0$). The Polyakov loop together with finite β effects strongly suppresses the critical temperature T_c in the second-order/crossover region at small μ, while it gives a minor modification of the first-order phase boundary at larger μ. As a result, the chiral phase boundary becomes much closer to the expected one in the real-life QCD as summarized in Fig. 12 (NLO case) and Fig.17 (left: NNLO, right NLO). It is also remarkable that the NNLO effects are subdominant in whole region of the phase diagram.

In both Haar measure MFA and Weiss MFAs, the critical point (CP) tends to go into low T region with increasing β, and the second-order chiral phase boundary becomes dominant. This trend is also reported in the MDP simulations [31, 32] and supports the recent MC results based on the critical surface analysis [46]. However, the trend is opposite to the anomaly based expectation for $N_f = 4 > 2$ [47]. The anomaly effects in the staggered fermion formalism should be further investigated in future.

We have investigated thermodynamic quantities, which is of great interest in the study of EOS of quark matter, which has however been challenging in SC-LQCD. Our findings are that a pressure and an interaction measure are drastically enhanced by Polyakov loop thermal excitations.

We have found some characteristic features of Polyakov loops at finite μ. At finite μ in the broken phase, the anti-Polyakov loop $\bar{\ell}$ becomes larger than ℓ, which is interpreted as a screening effect of quarks at equilibrium with net quark number density. In the chirally symmetric high density phase, the Polyakov loop becomes relatively large even at a small temperature, which can be understood from the absence of the dynamical quark mass in the symmetric phase.

We have shown that the chiral and Polyakov loop susceptibilities (χ_σ, χ_ℓ) have their peaks near to each other in the second-order transition or crossover region. In the vicinity of the critical point, the peak of the χ_ℓ rapidly diminishes. We have found two qualitative differences between the Weiss and Haar measure MFA on the Polyakov loop susceptibilities: First, the peak of χ_ℓ is more strongly locked to the chiral phase boundary in Weiss MFA than the Haar measure MFA case. Second, the Z_3 deconfinement dynamics artificially remains in the Haar measure MFA and disappears by taking account of the Polyakov loop fluctuations in Weiss MFA. Our findings are summarized in Fig. 8 (upper, Haar measure MFA result) and 8 (Weiss MFA result). The above difference results from the fact that the effective potential of Weiss MFA does not admit any remnant of the Z_3 symmetric structure in sharp contrast to the Haar measure MFA and many other chiral effective models [37, 43, 44]. Thus, the Weiss MFA does not support the isolated deconfinement transition/crossover from the chiral phase boundary at large μ.

There are several future directions to be investigated. First,

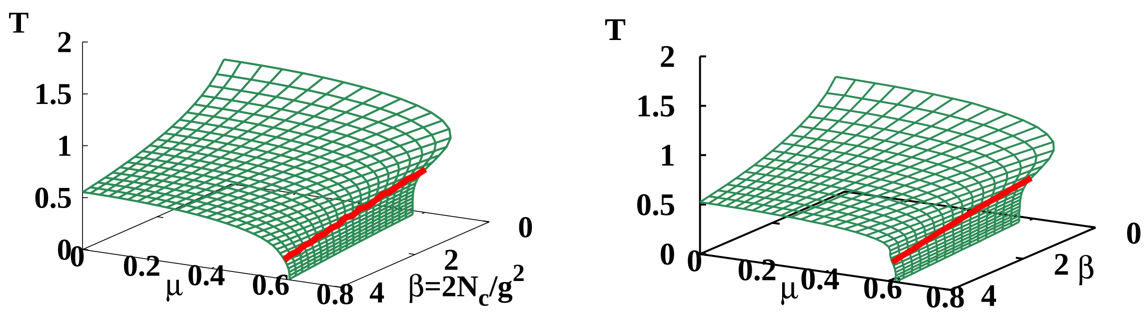

FIG. 17: (Color online) The phase diagram evolution for $m_0 = 0.05$ as a function of β in NNLO Haar-measure MFA (left), which is compared with the counterpart in NLO Haar-measure MFA (right) with same parameters. The red-thick-solid line represents the CEP evolution.

it is important to evaluate the higher order terms of the strong-coupling expansion, and/or to invent a resummation technique to account for the higher orders. From this viewpoint, we find recent developments for the Polyakov loop effective potential [48]. Second, it is desirable to establish the exact evaluation of each order of the strong-coupling expansion beyond the mean-field approximation and $1/d$ expansion. This will be achieved by extending the MDP works [31, 32] to include the higher-order of expansions as well as the Polyakov loop effects. Another method to go beyond MFA is the Monte-Carlo simulations for the auxiliary field integrals at each order of the expansion [33]. Third, it is interesting to evaluate the complex phase effect of Polyakov loops; The susceptibilities associated with the phase may give a new probe of the QCD phase transition [49]. And finally, the Weiss MFA results, especially the quark and Polyakov loop thermal excitations summarized in Table V, may open a possibility to invent an upgraded version of the PNJL-type model which more reasonably describes the interplay between the chiral and deconfinement dynamics.

Acknowledgments

We thank Maria Paola Lombardo and Philippe de Forcrand for fruitful discussions. This work was supported in part by the Grants-in-Aid for Scientific Research from JSPS (Nos. 22-3314, 15K05079, 15H03663, 16K05350), for Young Scientists (B) No.15K17644 (Kohtaroh Miura), the Grants-in-Aid for Scientific Research on Innovative Areas from MEXT (Nos. 24105001, 24105008), and the Yukawa International Program for Quark-hadron Sciences (YIPQS). Kohtaroh Miura is supported by the OCEVU Labex (ANR-11-LABX-0060) and the A*MIDEX project (ANR-11-IDEX-0001-02), funded by the "Investissements d'Avenir" French government program and managed by the ANR.

Appendix A: Effective potential in strong-coupling lattice QCD

We briefly review the derivation of the effective potential Eq. (1) based on our previous papers [27, 28]. We start from the lattice QCD action with one species of staggered fermion (χ) with a current quark mass (m_0) and chemical potential (μ),

TABLE I: The hadronic composites which appears after the spatial link integrals.

Symbol	Composites
M_x	$\bar\chi_x\chi_x$
$(V_x^+,\ V_x^-)$	$(\bar\chi_x e^{\mu}U_{0,x}\chi_{x+\hat 0},\ \bar\chi_{x+\hat 0}e^{-\mu}U_{0,x}^\dagger\chi_x)$
(W_x^+, W_x^-)	$(\bar\chi_x e^{2\mu}U_{0,x}U_{0,x+\hat 0}\chi_{x+2\hat 0},\ \bar\chi_{x+2\hat 0}e^{-2\mu}U_{0,x+\hat 0}^\dagger U_{0,x}^\dagger\chi_x)$
$L_{p,\mathbf{x}}$	$\mathrm{tr}_c\left[\prod_\tau U_{0,\mathbf{x}\tau}\right]/N_c$

$$\mathcal{Z}_{\rm LQCD} = \int \mathcal{D}[\chi,\bar\chi,U_\nu]\; e^{-S_{\rm LQCD}[\chi,\bar\chi,U_\nu]}\ , \tag{A1}$$

$$S_{\rm LQCD} = S_F + S_G + m_0\sum_x \bar\chi_x\chi_x\ , \tag{A2}$$

where,

$$S_F = \frac{1}{2}\sum_{\nu,x}\left[\eta_{\nu,x}\bar\chi_x U_{\nu,x}\chi_{x+\hat\nu} - \eta_{\nu,x}^{-1}(h.c.)\right]\ , \tag{A3}$$

$$\eta_{\nu,x} = \exp(\mu\,\delta_{\nu 0})(-1)^{x_0+\cdots+x_{\nu-1}}\ , \tag{A4}$$

$$S_G = \beta\sum_P\left[1 - \frac{1}{2N_c}\left[U_P + U_P^\dagger\right]\right]\ . \tag{A5}$$

We have employed lattice units $a = 1$. The $U_{\nu,x} \in SU(N_c)$ and $U_{P=\mu\nu,x} = \mathrm{tr}_c[U_{\mu,x}U_{\nu,x+\hat\mu}U_{\mu,x+\hat\nu}^\dagger U_{\nu,x}^\dagger]$ represent the link- and plaquette-variable, respectively. In the chiral limit ($m_0 \to 0$), the action has the $U_\chi(1)$ chiral symmetry, which is enhanced to $SU(N_f = 4)$ in the continuum limit.

There are four main steps to derive the effective potential from the lattice QCD action (A1) [28]: First, we carry out the strong-coupling expansion, and integrate out the spatial link variables in each order. The effective action is obtained as a function of various hadronic composites. For the composites including the staggered quarks ($\chi, \bar\chi$), we take account

TABLE II: The auxiliary field Φ and $(\ell, \bar{\ell})$ See also Table I.

Symbol	Mean Fields Contents
σ	$-\langle M\rangle$
$(\bar{\psi}_{\tau\tau}, \psi_{\tau\tau})$	$(\langle W^+\rangle,\ \langle W^-\rangle)$
$(\bar{\psi}_{ss}, \psi_{ss})$	$(\langle MM\rangle,\ \langle MMMM\rangle)$
$(\bar{\psi}_{\tau s}, \psi_{\tau s})$	$(-\langle V^+V^-\rangle,\ 2\langle MM\rangle)$
$(\bar{\psi}_{\tau}, \psi_{\tau})$	$(-\langle V^+\rangle,\ \langle V^-\rangle)$
$(\bar{\psi}_{s}, \psi_{s})$	$(\langle MM\rangle,\ \langle MM\rangle)$
$(\ell, \bar{\ell})$	$(\langle L_p\rangle, \langle \bar{L}_p\rangle)$

TABLE III: The coupling coefficients appearing in the effective action/potential. Here, g, $N_c = 3$, and $d = 3$ represents the gauge coupling, number of color, and spatial dimension, respectively. See Table II for the auxiliary fields $(\psi..., \bar{\psi}...)$.

Symbol	Definition
b_σ	$d/(2N_c)$
β_t	$\left(d/(N_c^2 g^2)\right)\cdot\left(1+1/(2g^2)\right)$
β_s	$\left(d(d-1)/(8N_c^4 g^2)\right)\cdot\left(1+1/(2g^2)\right)$
b'_σ	$b_\sigma + 2\left[\beta_{ss}\psi_{ss} + \beta_{\tau s}\bar{\psi}_{\tau s} + \beta'_s(\psi_s+\bar{\psi}_s)\right]$
β'_t	$\beta_t + \beta_{\tau s}\psi_{\tau s}$
β'_s	$\beta_s + 2\beta_{ss}\bar{\psi}_{ss}$
$\beta_{\tau\tau}$	$d/(2N_c^3 g^4)$
β_{ss}	$d(d-1)(d-2)/(16N_c^7 g^4)$
$\beta_{\tau s}$	$d(d-1)/(2N_c^5 g^4)$

of the terms up to $\mathcal{O}(1/g^6)$, and extract from them the leading order terms of the $1/d$ expansion $\mathcal{O}(1/d^0)$ [50]. For the pure gluonic composites, we take account of the leading order contributions to the Polyakov-loop $[\mathcal{O}(1/g^{2N_\tau}),\ N_\tau$: lattice temporal extension]. The hadronic composites are summarized in Table I, and the effective action is expressed by using these composites,

$$S_{\rm eff} = S_{\rm eff}^{\rm NNLO} + S_{\rm eff}^{\rm Pol}\ , \tag{A6}$$

with

$$S_{\rm eff}^{\rm Pol} = -N_c^2\left(\frac{1}{g^2 N_c}\right)^{N_\tau=1/T}\sum_{j,\mathbf{x}}\left[\bar{L}_{p,\mathbf{x}}L_{p,\mathbf{x}+\hat{j}} + h.c.\right]\ , \tag{A7}$$

TABLE IV: Quantities which govern the property of the effective potential. See Table III for the couplings $(b'_\sigma, \beta'_\tau, \beta_{\tau\tau})$ and Table II for the auxiliary fields $(\sigma, \psi_\tau, \bar{\psi}_\tau, \psi_{\tau\tau}, \bar{\psi}_{\tau\tau})$.

Symbol	Definition	Meanings
$\tilde{m}_q$	$m'_q/\sqrt{Z_+Z_-}$ $m'_q = b'_\sigma\sigma + m_0$ $-\beta_{\tau\tau}(\bar{\psi}_{\tau\tau}+\psi_{\tau\tau})$	dynamical quark mass
$\sqrt{Z_+Z_-}$	$Z_+ = 1+\beta'_\tau\bar{\psi}_\tau$ $+4\beta_{\tau\tau}m'_q\bar{\psi}_{\tau\tau}$ $Z_- = 1+\beta'_\tau\psi_\tau$ $+4\beta_{\tau\tau}m'_q\psi_{\tau\tau}$	wave function renormalization factor
E_q	$\sinh^{-1}\tilde{m}_q$	quark excitation energy
$\tilde{\mu}$	$\mu - \log\sqrt{Z_+/Z_-}$	shifted chemical potential

and

$$\begin{aligned}
S_{\rm eff}^{\rm NNLO} =& \sum_x \frac{1}{2}(V_x^+ - V_x^-) + \sum_{x,j>0}\Bigg[-\frac{b_\sigma}{2d}[MM]_{j,x}\\
&+\frac{\beta_\tau}{4d}[V^+V^- + V^-V^+]_{j,x} - \sum_{k>0,k\neq j}\frac{\beta_s[MMMM]_{jk,x}}{2d(d-1)}\\
&-\frac{\beta_{\tau\tau}}{2d}[W^+W^- + W^-W^+]_{j,x}\\
&+\sum_{|k|\neq j}\Bigg[\sum_{\substack{|k|,|l|>0,\\ |l|\neq j,|l|\neq|k|}}\frac{-\beta_{ss}[MMMM]_{jk,x}[MM]_{j,x+\hat{l}}}{4d(d-1)(d-2)}\\
&+\frac{\beta_{\tau s}[V^+V^- + V^-V^+]_{j,x}}{8d(d-1)}\\
&\quad\times\left([MM]_{j,x+\hat{k}} + [MM]_{j,x+\hat{k}+\hat{0}}\right)\Bigg]\Bigg]\ .
\end{aligned}\tag{A8}$$

We have introduced a short-hand notation

$$[AB]_{j,x} = A_x B_{x+\hat{j}}\ , \tag{A9}$$

$$[ABCD]_{jk,x} = A_x B_{x+\hat{j}} C_{x+\hat{j}+\hat{k}} D_{x+\hat{k}}\ , \tag{A10}$$

and the couplings $\beta...$ in Eq. (A8) are summarized in Table III.

Second, we introduce the auxiliary fields for the hadronic composites to bosonize the effective action $S_{\rm eff}^{\rm NNLO}$, and perform the static mean-field and saddle-point approximations. The auxiliary fields are summarized in Table II, and the $S_{\rm eff}^{\rm NNLO}$ reduces into

$$S_{\rm eff}^{\rm NNLO} \simeq S_{\rm eff}^{\rm F} + S_{\rm eff}^{\rm X}\ , \tag{A11}$$

TABLE V: The thermal excitation effects $\mathcal{P}_n^I$ and $\mathcal{Q}^I$ in the quark determinant of the Weiss MFA, Eq. (A21). The left column represents the excitation channel with the label I in the text: $(\mathrm{M},\mathrm{B},\mathrm{Q},\mathrm{D})$ stands for (mesonic,baryonic,quark,diquark) excitation. The quark excitation energy E_q and modified chemical potential $\tilde{\mu}$ appearing in the third column are explained in TableIV. In the right column, I_n represents a modified Bessel function with the argument $x = 4dN_c\big(\beta/(2N_c^2)\big)^{1/T}\sqrt{\ell\bar{\ell}}$.

Excitation (I)	N_{B}^I	$\mathcal{Q}^I(\Phi)$	$\mathcal{P}_n^I\left(\sqrt{\ell\bar{\ell}}\right)$
MMM	0	$\left(2\cosh(E_q/T)\right)^{N_c}$	$\mathcal{P}_n^{\mathrm{MMM}} = I_n^3 - I_{n-2}I_nI_{n+2} - 2I_{n-1}I_nI_{n+1} + I_{n-2}I_{n+1}^2 + I_{n-1}^2I_{n+2}$
MQQ̄	0	$2\cosh(E_q/T)$	$\mathcal{P}_n^{\mathrm{MQ\bar{Q}}} = -2(I_n^3 - I_{n-2}I_nI_{n+2}) + 5I_{n-1}I_nI_{n+1} - 3(I_{n-2}I_{n+1}^2 + I_{n-1}^2I_{n+2})$ $-I_{n-3}I_nI_{n+3} + I_{n-1}I_{n-2}I_{n+3} + I_{n-3}I_{n+1}I_{n+2}$
B	3	$e^{N_c\tilde{\mu}/T}$	$\mathcal{P}_n^{\mathrm{B}} = \mathcal{P}_{n-1}^{\mathrm{MMM}}$
B̄	-3	$e^{-N_c\tilde{\mu}/T}$	$\mathcal{P}_n^{\bar{\mathrm{B}}} = \mathcal{P}_{n+1}^{\mathrm{MMM}}$
MMQ	1	$e^{\tilde{\mu}/T}\left(2\cosh(E_q/T)\right)^2$	$\mathcal{P}_n^{\mathrm{MMQ}} = I_{n-1}I_n^2 + I_{n-3}I_{n+1}^2 - I_{n-1}^2I_{n+1} + I_{n-2}I_{n-1}I_{n+2} - I_{n-3}I_nI_{n+2} - I_{n-2}I_nI_{n+1}$
MMQ̄	-1	$e^{-\tilde{\mu}/T}\left(2\cosh(E_q/T)\right)^2$	$\mathcal{P}_n^{\mathrm{MM\bar{Q}}} = I_{n+1}I_n^2 + I_{n+3}I_{n-1}^2 - I_{n+1}^2I_{n-1} + I_{n-2}I_{n+1}I_{n+2} - I_{n+3}I_nI_{n-2} - I_{n+2}I_nI_{n-1}$
MD	2	$e^{2\tilde{\mu}/T}\ 2\cosh(E_q/T)$	$\mathcal{P}_n^{\mathrm{MD}} = \mathcal{P}_{n-1}^{\mathrm{MM\bar{Q}}}$
MD̄	-2	$e^{-2\tilde{\mu}/T}\ 2\cosh(E_q/T)$	$\mathcal{P}_n^{\mathrm{M\bar{D}}} = \mathcal{P}_{n+1}^{\mathrm{MMQ}}$
DQ̄	1	$e^{\tilde{\mu}/T}$	$\mathcal{P}_n^{\mathrm{D\bar{Q}}} = 2(I_{n-1}^2I_{n+1} - I_{n-2}I_{n-1}I_{n+2} + I_{n-3}I_nI_{n+2})$ $+I_{n-2}^2I_{n+3} - I_{n-1}I_n^2 - I_{n-3}I_{n+1}^2 - I_{n-3}I_{n-1}I_{n+3}$
QD̄	-1	$e^{-\tilde{\mu}/T}$	$\mathcal{P}_n^{\mathrm{Q\bar{D}}} = 2(I_{n+1}^2I_{n-1} - I_{n-2}I_{n+1}I_{n+2} + I_{n-2}I_nI_{n+3})$ $+I_{n+2}^2I_{n-3} - I_{n+1}I_n^2 - I_{n+3}I_{n-1}^2 - I_{n-3}I_{n+1}I_{n+3}$

where

$$S_{\mathrm{eff}}^{\mathrm{F}} = \sqrt{Z_+Z_-}\sum_{xy}\bar{\chi}_x G_{xy}^{-1}(\tilde{m}_q,\tilde{\mu})\chi_y\ , \tag{A12}$$

$$G_{xy}^{-1}(\tilde{m}_q,\tilde{\mu}) = \tilde{m}_q\delta_{xy} + \frac{\delta_{\mathbf{xy}}}{2}\left[e^{\tilde{\mu}}U_{0,x}\delta_{x+\hat{0},y} - e^{-\tilde{\mu}}U_{0,x}^\dagger\delta_{x-\hat{0},y}\right]\ , \tag{A13}$$

$$S_{\mathrm{eff}}^{\mathrm{X}} = N_\tau N_s^d\left[b_\sigma'\sigma^2 + \frac{1}{2}\beta_\tau'\bar{\psi}_\tau\psi_\tau + \frac{1}{2}\beta_s'\bar{\psi}_s\psi_s + \beta_{\tau\tau}\bar{\psi}_{\tau\tau}\psi_{\tau\tau} + \beta_{ss}\bar{\psi}_{ss}\psi_{ss} + \frac{1}{2}\beta_{\tau s}\bar{\psi}_{\tau s}\psi_{\tau s}\right]\ . \tag{A14}$$

Here, the dynamical quark mass $\tilde{m}_q$, the shifted quark chemical potential $\tilde{\mu}$, and the wave function renormalization factor $\sqrt{Z_+Z_-}$ are summarized in Table IV, and the $N_{t(s)}$ represents the temporal (spatial) lattice extension.

Third, we carry out the Gaussian integral over the staggered quarks $(\chi,\bar{\chi})$ in Eq. (A12) in the anti-periodic boundary condition. The resultant quark determinant at finite T is then calculated by using the Matsubara method in the Polyakov gauge for temporal link variables [42],

$$\int \mathrm{D}[\chi,\bar{\chi}]\, e^{-S_{\mathrm{eff}}^{\mathrm{F}}} = \prod_{\mathbf{x}}\left[e^{N_c(\log\sqrt{Z_+Z_-}+E_q)/T} \times \det{}_c\left[\left(1 + N_cL_{p,\mathbf{x}}e^{-(E_q-\tilde{\mu})/T}\right)\left(1 + N_c\bar{L}_{p,\mathbf{x}}e^{-(E_q+\tilde{\mu})/T}\right)\right]\right]\ , \tag{A15}$$

with $E_q = \sinh^{-1}\tilde{m}_q$. Temperature T is now considered as a continuous valued number (see the appendix in Ref. [24] for details). The Polyakov loop $L_{p,\mathbf{x}}$ has appeared in the determinant via the quark hopping wrapping around the temporal direction in addition to the Plaquette effects Eq. (A7).

Finally, we evaluate the $L_{p,\mathbf{x}}$ effects in the path integral over the temporal link variable U_0 in two approximation schemes: Haar measure and Weiss MFA. In the former, we replace the Polyakov loop $L_{p,\mathbf{x}}$ contained in Eq. (A7) and (A15) as well as the Haar measure of the U_0 path integral with a constant mean-field $(\ell,\bar{\ell})$ instead of performing the U_0 path integral. In the latter, we introduce a mean-field $(\ell,\bar{\ell})$ via the extended Hubbard-Stratonovich transformation [25] in Eq. (A7), and exactly carry out the U_0 path integral to include the fluctuation effects from $(\ell,\bar{\ell})$ [28].

As a result, we obtain the effective potential

$$\mathcal{F}_{\mathrm{eff}}^{\mathrm{H/W}}(\Phi,\ell,\bar{\ell};\beta,m_0,T,\mu) = \mathcal{F}_{\mathrm{X}}(\Phi,\beta) + \mathcal{F}_{\mathrm{det}}^{\mathrm{H/W}}(\Phi,\beta,m_0,T,\mu) + \mathcal{F}_{\mathrm{P}}^{\mathrm{H/W}}(\ell,\bar{\ell},\beta,T) + \mathcal{O}(1/g^6,1/\sqrt{d})\ . \tag{A16}$$

The auxiliary field term is given by Eq. (A14) and common in both Haar measure MFA and Weiss MFA,

$$\mathcal{F}_{\mathrm{X}}(\Phi,\beta) = S_{\mathrm{eff}}^{\mathrm{X}}/(N_tN_s^3)\ . \tag{A17}$$

The quark determinant and the Polyakov loop effects are given as

$$\mathcal{F}^{\rm H}_{\rm det} = -N_c E_q - N_c \log\sqrt{Z_+ Z_-} - T\Big(\log\mathcal{R}_q(E_q-\tilde{\mu},\ell,\bar{\ell}) + \log\mathcal{R}_q(E_q+\tilde{\mu},\bar{\ell},\ell)\Big)\ , \tag{A18}$$

$$\mathcal{R}_q(x,y,\bar{y}) \equiv 1 + N_c(ye^{-x/T}+\bar{y}e^{-2x/T}) + e^{-3x/T}$$

$$\mathcal{F}^{\rm H}_{\rm P} = -2TdN_c^2\left(\frac{1}{g^2N_c}\right)^{1/T}\bar{\ell}\ell - T\log\mathcal{R}_{\rm Haar}(\ell,\bar{\ell})\ , \tag{A19}$$

$$\mathcal{R}_{\rm Haar}(\ell,\bar{\ell}) \equiv 1 - 6\bar{\ell}\ell - 3\big(\bar{\ell}\ell\big)^2 + 4\big(\ell^{N_c}+\bar{\ell}^{N_c}\big)\ , \tag{A20}$$

in Haar measure MFA case, and

$$\mathcal{F}^{\rm W}_{\rm P} + \mathcal{F}^{\rm W}_{\rm det} = 2TdN_c^2\left(\frac{1}{g^2N_c}\right)^{1/T}\bar{\ell}\ell - T\log\left[\sum_I \mathcal{Q}^I(\Phi)\mathcal{P}^I(\ell,\bar{\ell})\right]\ , \tag{A21}$$

$$\mathcal{P}^I(\ell,\bar{\ell}) = \sum_{n=-\infty}^{\infty}\left(\sqrt{\ell/\bar{\ell}}\right)^{-N_cn+N_{\rm B}^I}\mathcal{P}^I_n\left(\sqrt{\ell\bar{\ell}}\right)\ , \tag{A22}$$

in Weiss MFA case. In Eqs. (A21) and (A22), the index I labels a pattern of thermal excitations of the quark composites, and the fermionic thermal excitation effects $\mathcal{Q}^I$, the Polyakov loop thermal excitation effects $\mathcal{P}^I_n$, and the baryon number index $N^I_{\rm B}$ are summarized in Table V.

As indicated in Eq. (A19) and (A21), the Z_3 symmetric term remains in the Haar measure MFA, but not in the Weiss MFA up to the first $\bar{\ell}\ell$ term. In the latter, the path integral over the temporal link variable U_0 which accounts for the summation over the Polyakov loop fluctuations spoils the Z_3 symmetry in the presence of the dynamical quarks. In heavy quark mass limit $m_0 \to \infty$, the Z_3 symmetry recovers in the Weiss MFA as follows: In the effective potential of Weiss MFA, the factor $\left(\sqrt{\ell/\bar{\ell}}\right)^{-N_cn+N^I_{\rm B}}$ in Eq. (A22) gives a unique source of the explicit Z_3 symmetry breaking ($(\ell,\bar{\ell}) \to (\Omega\ell,\Omega^{-1}\bar{\ell})$, $\Omega \in Z_3$). For $m_0 \to \infty$ or equivalently $E_q \gg T,\mu$, the three mesonic thermal excitation $\mathcal{Q}^{I={\rm MMM}}$ in Table V becomes dominant, and it does not carry the baryon number $N_{\rm B}^{I={\rm MMM}} = 0$. Therefore, the Eq. (11) reduces to

$$\mathcal{F}^{\rm W}_{\rm P} + \mathcal{F}^{\rm W}_{\rm det} = 2TdN_c^2\left(\frac{1}{g^2N_c}\right)^{1/T}\bar{\ell}\ell - T\log\Bigg[\mathcal{Q}^{I={\rm MMM}}(\Phi) \times \sum_{n=-\infty}^{\infty}\left(\sqrt{\ell/\bar{\ell}}\right)^{-N_cn}\mathcal{P}_n^{I={\rm MMM}}\left(\sqrt{\ell\bar{\ell}}\right)\Bigg]\ . \tag{A23}$$

This expression is invariant under the Z_3 transformation, $(\ell,\bar{\ell}) \to (\Omega\ell,\Omega^{-1}\bar{\ell})$ with the property $\Omega^{N_cn} = \mathbf{1}$ for $N_c = 3$.

Finally, we consider the confinement limit ($\ell,\bar{\ell} \to 0$) in the Weiss MFA. The quark determinant effect (A21) includes the Polyakov loop thermal excitation $\mathcal{P}^I_n$, which are solely characterized by the nth-order modified Bessel functions as shown in Table V. In the limit ($\ell,\bar{\ell} \to 0$), the 0th-order modified Bessel function remains finite ($I_0(x \to 0) = 1$) while the others vanishes ($I_{n\neq 0}(x \to 0) = 0$). Consequently, the only thermal excitations which carry the baryon number 0 and ± 3 survives in Table V, and the effective potential reduces into the one which we have derived in our previous work [25],

$$\mathcal{F}^{\rm W}_{\rm eff}(\Phi,\ell,\bar{\ell};\beta,m_0,T,\mu)|_{\ell,\bar{\ell}=0} \to \mathcal{F}^{\rm NLO}_{\rm eff}(\Phi;\beta,m_0,T,\mu) = \mathcal{F}_{\rm X}(\Phi,\beta) - T\log\left[\left(2\cosh\frac{E_q}{T}\right)^{N_c} - 4\cosh\frac{E_q}{T} + 2\cosh\frac{N_c\tilde{\mu}}{T}\right]\ . \tag{A24}$$

[1] For a recent lattice review of the QCD at finite temperature and/or density, see O. Philipsen, Prog. Part. Nucl. Phys. **70**, 55 (2013).

[2] For a recent review of the QCD phase diagram, see K. Fukushima and C. Sasaki, Prog. Part. Nucl. Phys. **72**, 99 (2013).

[3] For recent results and reviews, see, S. Borsanyi, Z. Fodor, C. Hoelbling, S. D. Katz, S. Krieg, C. Ratti and K. K. Szabo [Wuppertal-Budapest Collaboration], J. High Energy Phys. **1009**, 073 (2010).

[4] D. Bailin and A. Love, Phys. Rept. **107**, 325 (1984); R. Rapp, T. Schafer, E. V. Shuryak and M. Velkovsky, Phys. Rev. Lett. **81**, 53 (1998); M. G. Alford, K. Rajagopal and F. Wilczek, Phys. Lett. B **422**, 247 (1998); M. G. Alford, Ann. Rev. Nucl. Part. Sci. **51**, 131 (2001); D. T. Son, Phys. Rev. D **59**, 094019 (1999); M. G. Alford, K. Rajagopal and F. Wilczek, Nucl. Phys. B **537**, 443 (1999); J. Berges and K. Rajagopal, Nucl. Phys. B **538**, 215 (1999); K. Iida and G. Baym, Phys. Rev. D **63**, 074018 (2001) [Erratum-ibid. D **66**, 059903 (2002)]; M. Iwasaki and T. Iwado, Phys. Lett. B **350**, 163 (1995).

[5] L. McLerran and R. D. Pisarski, Nucl. Phys. A **796**, 83 (2007).

[6] Y. Hidaka, L. D. McLerran and R. D. Pisarski, Nucl. Phys. A **808**, 117 (2008); L. McLerran, K. Redlich and C. Sasaki, Nucl. Phys. A **824**, 86 (2009).

[7] L. McLerran, Nucl. Phys. A **830**, 709C (2009).

[8] T. Kojo, Y. Hidaka, K. Fukushima, L. D. McLerran and R. D. Pisarski, Nucl. Phys. A **875**, 94 (2012); T. Kojo, Y. Hidaka, L. McLerran and R. D. Pisarski, Nucl. Phys. A **843**, 37 (2010).

[9] For a recent review, see, C. Gale, S. Jeon and B. Schenke, Int. J. Mod. Phys. A **28**, 1340011 (2013).

[10] M. Asakawa and K. Yazaki, Nucl. Phys. A **504**, 668 (1989); M. A. Stephanov, K. Rajagopal and E. V. Shuryak, Phys. Rev. Lett. **81**, 4816 (1998).

[11] B. Mohanty [STAR Collaboration], J. Phys. G **38**, 124023 (2011) [arXiv:1106.5902 [nucl-ex]].

[12] For a review of a finite chemical potential on lattice, see S. Muroya, A. Nakamura, C. Nonaka and T. Takaishi, Prog. Theor. Phys. **110**, 615 (2003).

[13] G. Aarts, PoS LATTICE **2012**, 017 (2012) [arXiv:1302.3028 [hep-lat]].

[14] H. Fujii, D. Honda, M. Kato, Y. Kikukawa, S. Komatsu and T. Sano, JHEP **1310**, 147 (2013) [arXiv:1309.4371 [hep-lat]].

[15] M. Cristoforetti *et al.* [AuroraScience Collaboration], Phys.

Rev. D **86**, 074506 (2012) [arXiv:1205.3996 [hep-lat]].
[16] The review of the pioneering works for the strong-coupling expansion is found in the text book, I. Montvay and G. Münster, “Quantum Fields on a Lattice,” Cambridge University Press, 1994; M. Creutz, “Quarks, Gluons, and Lattices,” Cambridge Univ. Press, 1983.
[17] K. G. Wilson, Phys. Rev. D **10**, 2445 (1974).
[18] M. Creutz, Phys. Rev. D **21**, 2308 (1980); M. Creutz and K. J. M. Moriarty, Phys. Rev. D **26**, 2166 (1982).
[19] G. Münster, Nucl. Phys. B **180**, 23 (1981).
[20] K. Fukushima, Prog. Theor. Phys. Suppl. **153**, 204 (2004).
[21] Y. Nishida, K. Fukushima and T. Hatsuda, Phys. Rept. **398**, 281 (2004).
[22] Y. Nishida, Phys. Rev. D **69**, 094501 (2004).
[23] V. Azcoiti, G. Di Carlo, A. Galante and V. Laliena, J. High Energy Phys. **09**, 014 (2003).
[24] N. Kawamoto, K. Miura, A. Ohnishi and T. Ohnuma, Phys. Rev. D **75**, 014502 (2007).
[25] K. Miura, T. Z. Nakano, A. Ohnishi and N. Kawamoto, Phys. Rev. D **80**, 074034 (2009); K. Miura, T. Z Nakano and A. Ohnishi, Prog. Theor. Phys. **122**, 1045 (2009).
[26] K. Miura, T. Z. Nakano, A. Ohnishi and N. Kawamoto, arXiv:1106.1219 [hep-lat].
[27] T. Z. Nakano, K. Miura and A. Ohnishi, Prog. Theor. Phys. **123**, 825 (2010).
[28] T. Z. Nakano, K. Miura and A. Ohnishi, Phys. Rev. D **83**, 016014 (2011).
[29] B. Bringoltz, J. High Energy Phys. **03**, 016 (2007).
[30] P. de Forcrand and M. Fromm, Phys. Rev. Lett. **104**, 112005 (2010).
[31] P. de Forcrand, J. Langelage, O. Philipsen and W. Unger, arXiv:1406.4397 [hep-lat].
[32] P. de Forcrand, M. Fromm, J. Langelage, K. Miura, O. Philipsen and W. Unger, arXiv:1111.4677 [hep-lat]; P. de Forcrand, J. Langelage, O. Philipsen and W. Unger, arXiv:1312.0589 [hep-lat].
[33] T. Ichihara, A. Ohnishi and T. Z. Nakano, PTEP **2014** (2014), 123D02 [arXiv:1401.4647 [hep-lat]]; T. Ichihara, T. Z. Nakano and A. Ohnishi, Proc. Sci. LAT2013, 143 (2014); A. Ohnishi, T. Ichihara and T. Z. Nakano, Proc. Sci. LAT2012, 088 (2012).
[34] A. Gocksch and M. Ogilvie, Phys. Rev. D **31**, 877 (1985).
[35] E. M. Ilgenfritz and J. Kripfganz, Z. Phys. C **29**, 79 (1985).
[36] K. Fukushima, Phys. Rev. D **68**, 045004 (2003).
[37] K. Fukushima, Phys. Lett. B **591**, 277 (2004).
[38] P. de Forcrand, private communication: For the temporal lattice extension $N_t = 2$, the lattice bare coupling associated with the chiral phase transition (β_c) is found to be 3.67 at the bare quark mass $m_0 = 0.025$ and 3.81 at $m_0 = 0.05$ for one species of staggered fermion.
[39] G. Boyd, J. Fingberg, F. Karsch, L. Karkkainen and B. Petersson, Nucl. Phys. B **376**, 199 (1992); R. V. Gavai *et al.* [MT(c) Collaboration], Phys. Lett. B **241**, 567 (1990); S. A. Gottlieb, W. Liu, D. Toussaint, R. L. Renken and R. L. Sugar, Phys. Rev. D **35**, 3972 (1987); A. D. Kennedy, J. Kuti, S. Meyer and B. J. Pendleton, Phys. Rev. Lett. **54**, 87 (1985).
[40] J. Engels, R. Joswig, F. Karsch, E. Laermann, M. Lutgemeier and B. Petersson, Phys. Lett. B **396**, 210 (1997).
[41] J. Polonyi and K. Szlachanyi, Phys. Lett. B **110**, 395 (1982); M. Gross, Phys. Lett. B **132**, 125 (1983); J. Bartholomew, D. Hochberg, P. H. Damgaard and M. Gross, Phys. Lett. B **133**, 218 (1983).
[42] P. H. Damgaard, N. Kawamoto and K. Shigemoto, Nucl. Phys. B **264**, 1 (1986).
[43] K. Fukushima, Phys. Rev. D **77**, 114028 (2008).
[44] T. K. Herbst, J. M. Pawlowski and B. J. Schaefer, Phys. Lett. B **696**, 58 (2011); Phys. Rev. D **88**, no. 1, 014007 (2013).
[45] T. Jolicoeur, H. Kluberg-Stern, M. Lev, A. Morel and B. Petersson, Nucl. Phys. B **235**, 455 (1984).
[46] P. de Forcrand and O. Philipsen, J. High Energy Phys. **0811**, 012 (2008).
[47] R. D. Pisarski and F. Wilczek, Phys. Rev. D **29**, 338 (1984).
[48] G. Bergner, J. Langelage and O. Philipsen, J. High Energy Phys. **1403**, 039 (2014); J. Langelage and O. Philipsen, J. High Energy Phys. **1004**, 055 (2010); J. High Energy Phys. **1001**, 089 (2010); J. Langelage, G. Munster and O. Philipsen, J. High Energy Phys. **0807**, 036 (2008).
[49] P. M. Lo, B. Friman, O. Kaczmarek, K. Redlich and C. Sasaki, Phys. Rev. D **88**, no. 1, 014506 (2013) [arXiv:1306.5094 [hep-lat]].
[50] H. Kluberg-Stern, A. Morel and B. Petersson, Nucl. Phys. B **215**, 527 (1983).
[51] In fact, the PNJL model is invented from the SC-LQCD [37].